









# Photochemistry of Anoxic Abiotic Habitable Planet Atmospheres: Impact of New H<sub>2</sub>O Cross Sections

Sukrit Ranjan<sup>1,2,10</sup> , Edward W. Schwieterman<sup>3,4,5</sup> , Chester Harman<sup>6</sup> , Alexander Fateev<sup>7</sup> , Clara Sousa-Silva<sup>1</sup> , Sara Seager<sup>1</sup>, and Renyu Hu<sup>8,9</sup> 

<sup>1</sup>Massachusetts Institute of Technology, 77 Massachusetts Avenue, Cambridge, MA 02140, USA; [sukrit@mit.edu](mailto:sukrit@mit.edu)

<sup>2</sup>Northwestern University, 1800 Sherman Avenue, Evanston, IL 60201, USA

<sup>3</sup>School of Earth and Atmospheric Sciences, Georgia Institute of Technology, Atlanta, GA 30332 USA

<sup>4</sup>Department of Earth and Planetary Sciences, University of California, Riverside, CA 92521 USA

<sup>5</sup>Blue Marble Space Institute of Science, Seattle, WA, USA

<sup>6</sup>NASA Ames Research Center, Moffett Field, CA 94035, USA

<sup>7</sup>Technical University of Denmark, Department of Chemical and Biochemical Engineering, Frederiksborgvej 399, Roskilde DK-4000, Denmark

<sup>8</sup>Jet Propulsion Laboratory, California Institute of Technology, Pasadena, CA 91109, USA

<sup>9</sup>Division of Geological and Planetary Sciences, California Institute of Technology, Pasadena, CA 91125, USA

Received 2020 March 4; revised 2020 May 12; accepted 2020 May 13; published 2020 June 23

## Abstract

We present a study of the photochemistry of abiotic habitable planets with anoxic CO<sub>2</sub>–N<sub>2</sub> atmospheres. Such worlds are representative of early Earth, Mars, and Venus and analogous exoplanets. Photodissociation of H<sub>2</sub>O controls the atmospheric photochemistry of these worlds through production of reactive OH, which dominates the removal of atmospheric trace gases. The near-UV (NUV; >200 nm) absorption cross sections of H<sub>2</sub>O play an outsized role in OH production; these cross sections were heretofore unmeasured at habitable temperatures (<373 K). We present the first measurements of NUV H<sub>2</sub>O absorption at 292 K and show it to absorb orders of magnitude more than previously assumed. To explore the implications of these new cross sections, we employ a photochemical model; we first intercompare it with two others and resolve past literature disagreement. The enhanced OH production due to these higher cross sections leads to efficient recombination of CO and O<sub>2</sub>, suppressing both by orders of magnitude relative to past predictions and eliminating the low-outgassing “false-positive” scenario for O<sub>2</sub> as a biosignature around solar-type stars. Enhanced [OH] increases rainout of reductants to the surface, relevant to prebiotic chemistry, and may also suppress CH<sub>4</sub> and H<sub>2</sub>; the latter depends on whether burial of reductants is inhibited on the underlying planet, as is argued for abiotic worlds. While we focus on CO<sub>2</sub>-rich worlds, our results are relevant to anoxic planets in general. Overall, our work advances the state of the art of photochemical models by providing crucial new H<sub>2</sub>O cross sections and resolving past disagreement in the literature and suggests that detection of spectrally active trace gases like CO in rocky exoplanet atmospheres may be more challenging than previously considered.

*Unified Astronomy Thesaurus concepts:* Planetary theory (1258); Planetary atmospheres (1244); Exoplanet atmospheres (487); Exoplanet atmospheric composition (2021); Extrasolar rocky planets (511); Habitable planets (695); Water vapor (1791)

## 1. Introduction

The statistical finding that rocky, temperate exoplanets are common (Dressing & Charbonneau 2015) has received dramatic validation with the discovery of nearby potentially habitable worlds like LHS-1140b, TRAPPIST-1e, TOI-700d, and Kepler-442b (Torres et al. 2015; Dittmann et al. 2017; Gillon et al. 2017; Gilbert et al. 2020). Upcoming facilities such as the James Webb Space Telescope, the Extremely Large Telescopes, and the HabEx and LUVOIR mission concepts will have the ability to detect the atmospheres of such worlds and possibly characterize their atmospheric compositions (Rodler & López-Morales 2014; Fujii et al. 2018; Lustig-Yaeger et al. 2019; LUVOIR Team 2019; Meixner et al. 2019; Gaudi et al. 2020).

The prospects for rocky exoplanet atmospheric characterization have led to extensive photochemical modeling of their potential atmospheric compositions, with an emphasis on constraining the possible concentrations of spectroscopically active trace gases like CO, O<sub>2</sub>, and CH<sub>4</sub>. Particular emphasis has been placed on modeling the atmospheres of habitable but abiotic planets with anoxic, CO<sub>2</sub>–N<sub>2</sub> atmospheres (e.g., Harman et al. 2018; Hu et al. 2012, 2020; James & Hu 2018; Rimmer & Helling 2016;

Rugheimer et al. 2015b; Segura et al. 2007; Schwieterman et al. 2016). Such atmospheres are expected from outgassing on habitable terrestrial worlds; representative of early Earth, Mars, and Venus (Kasting 1993; Way et al. 2016; Wordsworth 2016); and expected on habitable exoplanets orbiting younger, fainter stars or at the outer edges of their habitable zones (e.g., TRAPPIST-1e; Kopparapu et al. 2013; Wolf 2017).

Water vapor plays a critical role in the photochemistry of such atmospheres because in anoxic abiotic atmospheres, H<sub>2</sub>O photolysis is the main source of the radical OH, which is the dominant sink of most trace atmospheric gases (Harman et al. 2015; Rugheimer et al. 2015a). Most water vapor is confined to the lower atmosphere due to the decline of temperature with altitude and the subsequent condensation of H<sub>2</sub>O, the “cold trap” (e.g., Wordsworth & Pierrehumbert 2013). In CO<sub>2</sub>-rich atmospheres, this abundant lower atmospheric H<sub>2</sub>O is shielded from UV photolysis at far-UV (FUV) wavelengths (≲200 nm),<sup>11</sup>

<sup>11</sup> The partitioning of the UV into NUV, FUV, and sometimes mid-UV (MUV) is highly variable (e.g., France et al. 2013; Domagal-Goldman et al. 2014; Shkolnik & Barman 2014; Harman et al. 2015). In this paper, we adopt the nomenclature of Harman et al. (2015) that NUV corresponds to >200 nm and FUV to ≲200 nm, because this partitioning approximately coincides with the onset of CO<sub>2</sub> absorption.

<sup>10</sup> SCOL Postdoctoral Fellow.

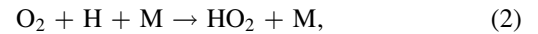
meaning that near-UV (NUV;  $>200$  nm) absorption plays an overweight role in  $\text{H}_2\text{O}$  photolysis (Harman et al. 2015). Therefore, the NUV absorption cross sections of  $\text{H}_2\text{O}$  are critical inputs to photochemical modeling of anoxic abiotic habitable planet atmospheres. However, to our knowledge, the NUV absorption of  $\text{H}_2\text{O}$  at habitable temperatures ( $<373$  K) was not known prior to this work. In the absence of measurements, photochemical models relied upon varying assumptions regarding  $\text{H}_2\text{O}$  NUV absorption (Kasting & Walker 1981; Sander et al. 2011; Rimmer & Helling 2016; Rimmer & Rugheimer 2019).

In this paper, we present the first-ever measurements of the NUV cross sections of  $\text{H}_2\text{O}(\text{g})$  at temperatures relevant to habitable worlds ( $T = 292 \text{ K} < 373 \text{ K}$ ) and explore the implications for the atmospheric photochemistry of abiotic habitable planets with anoxic  $\text{CO}_2\text{-N}_2$  atmospheres orbiting Sun-like stars. We begin by briefly reviewing the photochemistry of anoxic  $\text{CO}_2\text{-N}_2$  atmospheres and the key role of  $\text{H}_2\text{O}$  (Section 2). We proceed to measure the cross sections of  $\text{H}_2\text{O}(\text{g})$  in the laboratory and find it to absorb orders of magnitude more in the NUV than previously assumed by any model; this laboratory finding is consistent with our (limited) theoretical understanding of the behavior of the water molecule (Section 3). We incorporate these new cross sections into our photochemical model. Previous models of such atmospheres have been discordant; we conduct an intercomparison between three photochemical models to successfully reconcile this discordance to within a factor of  $2\times$  (Section 4). We explore the impact of our newly measured, larger  $\text{H}_2\text{O}$  cross sections and their concomitantly higher OH production on the atmospheric photochemistry and composition for our planetary scenario (Section 5). We focus on  $\text{O}_2$  and especially CO, motivated by their spectral detectability and proposed potential to discriminate the presence of life on exoplanets (Snellen et al. 2010; Brogi et al. 2014; Rodler & López-Morales 2014; Schwieterman et al. 2016, 2019; Wang et al. 2016; Krissansen-Totton et al. 2018; Meadows et al. 2018), but we consider the implications for other species as well, especially  $\text{CH}_4$  and  $\text{H}_2$ . We summarize our findings in Section 6. The Appendices contain supporting details: Appendix A details our simulation parameters, Appendix B details the boundary conditions, and Appendix C details our model intercomparison and the insights derived thereby. While we focus here on  $\text{CO}_2$ -rich atmospheres, our results are relevant to any planetary scenario in which  $\text{H}_2\text{O}$  photolysis is the main source of OH, which includes most anoxic atmospheric scenarios.

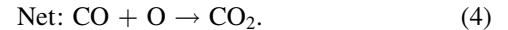
## 2. Photochemistry of $\text{CO}_2$ -rich Atmospheres

In this section, we briefly review the photochemistry of  $\text{CO}_2$ -rich atmospheres. For a more detailed discussion, we refer the reader to Catling & Kasting (2017).

Ultraviolet light readily dissociates atmospheric  $\text{CO}_2$  via  $\text{CO}_2 + h\nu \rightarrow \text{CO} + \text{O}$  ( $\lambda < 202$  nm; Ityaksov et al. 2008). The direct recombination of CO and O is spin forbidden and slow, and the reaction  $\text{O} + \text{O} + \text{M} \rightarrow \text{O}_2 + \text{M}$  is faster. Consequently,  $\text{CO}_2$  on its own is unstable to conversion to CO and  $\text{O}_2$  (Schaefer & Fegley 2011). However, OH can react efficiently with CO via the reaction  $\text{CO} + \text{OH} \rightarrow \text{CO}_2 + \text{H}$  and is the main photochemical control on CO and  $\text{O}_2$  via catalytic cycles such as



and



On Mars, such OH-driven catalytic cycles stabilize the  $\text{CO}_2$  atmosphere against conversion to CO and  $\text{O}_2$  (McElroy & Donahue 1972; Parkinson & Hunten 1972; Krasnopolsky 2011). These catalytic cycles are diverse but unified in requiring OH to proceed (Harman et al. 2018). Similarly, on modern Earth, OH is the main sink on CO (Badr & Probert 1995). On Venus, the products of HCl photolysis are thought to support this recombination (Prinn 1971; Yung & Demore 1982; Mills & Allen 2007; Sandor & Clancy 2018); however, this mechanism should not be relevant to habitable planets with hydrology, where highly soluble HCl should be efficiently scrubbed from the atmosphere (Prinn & Fegley 1987; Lightowers & Cape 1988).

On oxidic modern Earth, the main source of OH is the reaction  $\text{O}(\text{D}) + \text{H}_2\text{O} \rightarrow 2\text{OH}$ , with  $\text{O}(\text{D})$  sourced from  $\text{O}_3$  photolysis via  $\text{O}_3 + h\nu \rightarrow \text{O}(\text{D}) + \text{O}_2$  ( $\lambda < 320$  nm; Jacob 1999). However, on anoxic worlds,  $\text{O}_3$  is low, and OH is instead ultimately sourced from  $\text{H}_2\text{O}$  photolysis ( $\text{H}_2\text{O} + h\nu \rightarrow \text{OH} + \text{H}$ ), though it may accumulate in alternative reservoirs (Tian et al. 2014; Harman et al. 2015). Consequently, on anoxic abiotic worlds, the balance between  $\text{CO}_2$  and  $\text{H}_2\text{O}$  photolysis is thought to control the photochemical accumulation of CO in the atmosphere. The OH also reacts with a wide range of other gases. Hence, the photochemistry of  $\text{CO}_2$ -dominated atmospheres is controlled by  $\text{H}_2\text{O}$  through its photolytic product OH.

The proper operation of this so-called  $\text{HO}_x$  photochemistry in photochemical models is commonly tested by reproducing the atmosphere of modern Mars, which is controlled by these processes (e.g., Hu et al. 2012). However, the atmosphere on modern Mars is thin ( $\sim 0.006$  bar), whereas the atmospheres of potentially habitable worlds are typically taken to be more Earth-like ( $\sim 1$  bar). As we will show, models that are convergent in the thin atmospheric regime of modern Mars may become divergent for thicker envelopes, illustrating the need for intercomparisons in diverse regimes to assure model accuracy (Section 4). In particular, on planets with high  $\text{CO}_2$  abundance, the  $\text{H}_2\text{O}$ -rich lower atmosphere is shielded from FUV radiation by  $\text{CO}_2$ , meaning that  $\text{H}_2\text{O}$  photolysis at low altitudes is dependent on NUV photons.

In addition to the atmospheric sources and sinks discussed here, CO may have strong surface sources and sinks. In particular, impacts, outgassing from reduced melts, and biology may supply significant CO to the atmosphere, and biological uptake in the oceans may limit [CO] in some scenarios (Kasting 1990; Kharecha et al. 2005; Batalha et al. 2015; Schwieterman et al. 2019). In this work, we focus solely on photochemical CO and neglect these other sources and sinks.

## 3. Measurements of NUV $\text{H}_2\text{O}$ Cross Sections at 292 K

As discussed above, NUV  $\text{H}_2\text{O}$  photolysis is critical to the photochemistry of abiotic habitable planets with anoxic  $\text{CO}_2$ -rich atmospheres. However, prior to this work, no experimentally measured or theoretically predicted absorption cross sections were available for  $\text{H}_2\text{O}(\text{g})$  at habitable conditions ( $T < 373$  K) at wavelengths  $>198$  nm (Burkholder et al. 2015). This is because  $\text{H}_2\text{O}$  absorption cross sections are very weak

(<math>1 \times 10^{-20}</math> cm<sup>2</sup> at  $\geq 190$  nm), which makes their measurement difficult. Here we extend this coverage to 230 nm by measuring the absorption cross section of H<sub>2</sub>O(g) at 292 K between 186 and 230 nm (0.11 nm spectral resolution). We describe our method (Section 3.1), consider the consistency with past measurements and theoretical expectations, and prescribe H<sub>2</sub>O cross sections for inclusion in atmospheric models (Section 3.2).

### 3.1. Experimental Setup and Measurements

The measurements have been performed in a special flow gas cell. The cell is made from a stainless steel tube ( $\sim 25$  mm inner diameter) in a straight-line design and is 570 cm long. The cell is thermally isolated, and can be heated up to 200°C. Exchangeable sealed optical windows at both ends allow optical measurements in a wide spectral range from FUV to far-IR (defined by window material). In the present measurements, MgF<sub>2</sub> vacuum ultraviolet (VUV) windows have been used.

The cell is coated inside with SilcoNert 2000 coating,<sup>12</sup> which has good hydrophobic properties<sup>13</sup> and is very inert<sup>14</sup> to various reactive gases, allowing low-level optical absorption measurements (e.g., sulfur/H<sub>2</sub>S, NH<sub>3</sub>, formaldehyde, etc.) in various laboratory and industrial environments (e.g., analytical, stack, and process gases).

Flow through the cell is controlled with a high-end mass-flow controller (MFC; BRONKHORST). The pressure measurements in the cell were calibrated with a high-end ROSEMOUNT pressure sensor.

The NUV absorption measurements were done with a 0.5 m FUV spectrometer equipped with X-UV CCD (Princeton Instruments; spectral range 110–240 nm), FUV-coated collimating optics (mirrors) and a VUV D2 lamp (HAMAMATSU). The spectrometer and optics were purged with N<sub>2</sub> (99.999%). Because H<sub>2</sub>O has continuum-like absorption between 180–240 nm, the measurements have been done with a 600 grooves mm<sup>-1</sup> grating blazing at 150 nm without spectral scanning (spectral resolution  $\Delta\lambda = 0.11$  nm).

For H<sub>2</sub>O measurements, a gas-tight HAMILTON syringe<sup>15</sup> and an accurate syringe pump with a water evaporator (heated to 150°C) were used in order to produce controlled N<sub>2</sub>+H<sub>2</sub>O (1.5%–2%) mixtures. Milli-Q water,<sup>16</sup> purified from tap water, was used. We did not characterize the isotopic composition of our tap water but see no reason for the heavier isotopes of water to be absent. This means that our water vapor cross sections should include contributions from heavier isotopes of water, such as HDO and D<sub>2</sub>O. Since these heavier isotopes should be present on other planets as well, we argue our use of tap water to be appropriate for representative spectra of water vapor for planetary simulations. As a practical note, the finding of Chung et al. (2001) that  $\sigma_{\text{H}_2\text{O}}$  is significantly larger than  $\sigma_{\text{HDO}}$  and  $\sigma_{\text{D}_2\text{O}}$  for  $\lambda > 180$  nm, combined with the low absolute abundances of these heavier isotopes, indicates that their contribution to our measured NUV spectrum should be minimal. The water evaporation system (syringe + pump + evaporator) was the

same as previously used in high-temperature N<sub>2</sub>+H<sub>2</sub>O transmissivity measurements (Ren et al. 2015).

In the absorption measurements, cold N<sub>2</sub> (i.e., at 19°C) flowed into a heated evaporator, where H<sub>2</sub>O from a syringe pump was mixed in. The N<sub>2</sub> + H<sub>2</sub>O mixture then entered a 2 m unheated Teflon line (inner diameter 4 mm) connected to the cell, where the mixture naturally cooled down. The N<sub>2</sub> flow through the system was kept at 2  $l_n$  minute<sup>-1</sup> in all measurements ( $l_n$  minute<sup>-1</sup> = normal liter per minute). The effective residence time of the gas in the cell at that flow rate and 19.4°C was 1.31 minutes.

To account for any heat-transfer effects from the injection of cold N<sub>2</sub> through the heated evaporator and into the cell, reference measurements (i.e., without H<sub>2</sub>O(g)) were performed with N<sub>2</sub> at 99.999%. The outlet of the cell was kept open. The temperature in the cell was continuously measured in two zones with thermocouples. The temperature in the cell during the measurements was between 19.2°C and 19.7°C with temperature uniformity of  $\pm 0.1^\circ\text{C}$  at a particular measurement. It should be noted that the H<sub>2</sub>O saturation point at 19.2°C is 2.19 volume % at the conditions of the measurements. Therefore, all measurements with water were below saturation conditions. Prior to our measurements, we purged our apparatus with dry air (H<sub>2</sub>O- and CO<sub>2</sub>-free) for  $\sim 2$  days.

We conducted four measurement sequences of the H<sub>2</sub>O cross sections. In each of the first three measurement sequences, we began by taking a reference spectrum of dry N<sub>2</sub>. We then injected 1.5% water vapor into our apparatus and took five to six spectra of N<sub>2</sub>+1.5% H<sub>2</sub>O. We finished the sequence with another N<sub>2</sub> spectrum for a baseline check. In the fourth measurement sequence, we instead injected 2% water vapor into our apparatus, in order to get a better signal-to-noise ratio (S/N) in the 215–230 nm wavelength where H<sub>2</sub>O has the lowest absorption cross sections. The first of the five to six N<sub>2</sub>+H<sub>2</sub>O measurements in a sequence was performed to ensure that [H<sub>2</sub>O] was stable; it was discarded and did not contribute toward the cross-section calculations. We also discarded the first of the four sequences because the measurements were not stable; we attribute this to H<sub>2</sub>O saturating the surfaces of the dry system, which had been purged for days. Consequently, the final mean spectrum is based on three sequences of four to five measurements each, two at 1.5% H<sub>2</sub>O and one at 2.0% H<sub>2</sub>O.

Absorption cross sections were calculated assuming the Lambert–Beer law,

$$\tau(\lambda) = \ln \frac{I_0(\lambda)}{I_1(\lambda)}, \quad (5)$$

$$\sigma(\lambda) = \frac{\tau(\lambda)}{n_{\text{H}_2\text{O}}L}, \quad (6)$$

where

1.  $\lambda$  is the wavelength, specified in nm in our apparatus;
2.  $L$  is the path length in cm ( $L = 570$  cm in our apparatus);
3.  $n_{\text{H}_2\text{O}}$  is water concentration in molecules cm<sup>-3</sup> (defined by the amount of evaporated water, temperature, and pressure in the cell);
4.  $\sigma(\lambda)$  is the absorption cross section in cm<sup>2</sup> molecule<sup>-1</sup>;
5.  $\tau(\lambda)$  is the optical depth;
6.  $I_0(\lambda)$  is the reference spectrum (99.999% N<sub>2</sub> in the cell); and
7.  $I_1(\lambda)$  is the absorbance spectrum (99.999% N<sub>2</sub> + 1.5% or 2% H<sub>2</sub>O in the cell).

<sup>12</sup> Silcotek Company: <https://www.silcotek.com/silcod-technologies/silconert-inert-coating>.

<sup>13</sup> Silcotek hydrophobicity rating of “3.”

<sup>14</sup> Silcotek chemical inertness rating of “4.”

<sup>15</sup> Hamilton Company: <https://www.hamiltoncompany.com/laboratory-products/syringes/general-syringes/gastight-syringes/1000-series>.

<sup>16</sup> <https://dk.vwr.com/store/product/en/2983107/ultrarene-vandsystemer-milli-q-reference?languageChanged=en>

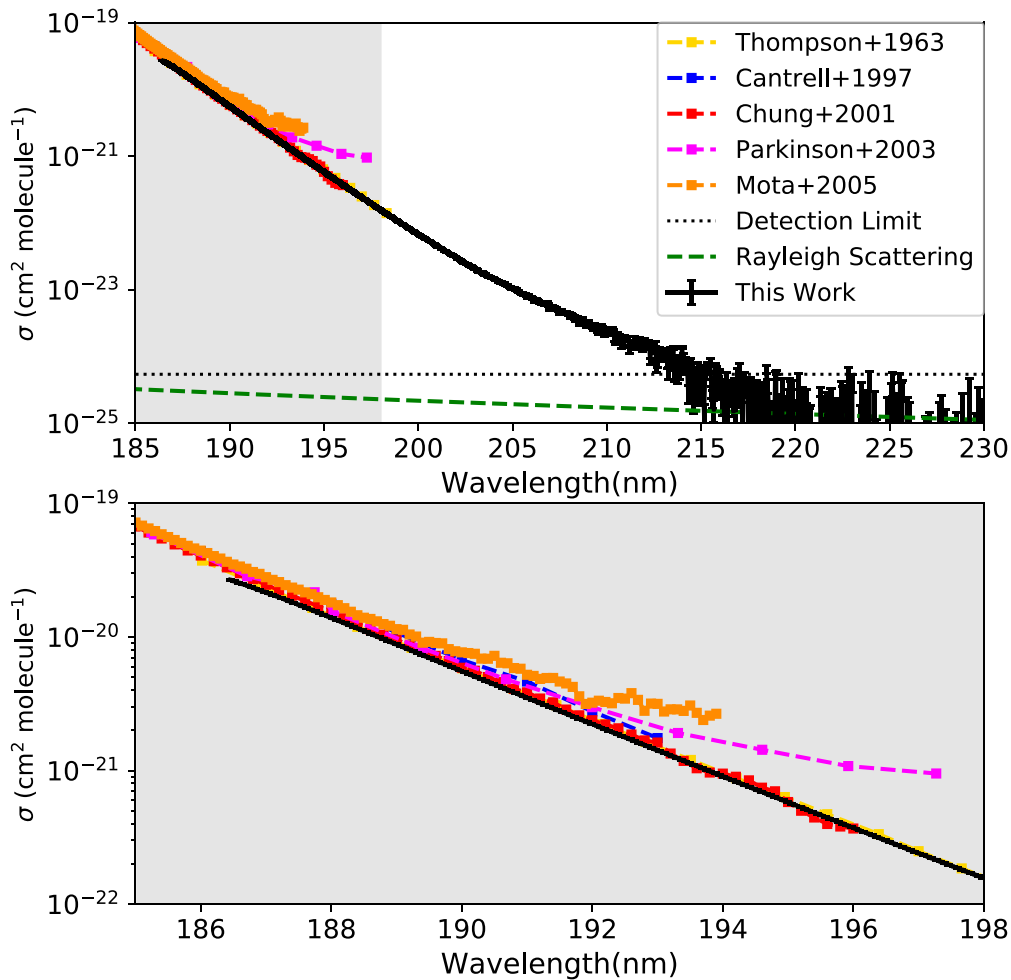


**Figure 1.** New  $\text{H}_2\text{O}$  absorption cross sections compared to published data. Also plotted is the Rayleigh scattering cross section, calculated as in Ranjan & Sasselov (2017). The top plot shows the full data set; the bottom zooms in on the 185–198 nm wavelength region (highlighted in gray in the top plot) where data for comparison are available. The dotted black line demarcates the detection limit of our apparatus (Section 3.1).

Both  $I_0(\lambda)$  and  $I_1(\lambda)$  are corrected for stray light in the system.

We averaged the measured cross sections from our three sequences of four to five measurements each to calculate a mean absorption spectrum and estimate its errors. Absorption cross sections are calculated with the use of Equation (5). Errors of the mean absorption cross sections are calculated taking into account the mean experimental standard deviations of the absorption spectra and standard deviations in pressure and water concentration measurements and calculations. The former is defined by the pressure sensor used, and the latter is defined by uncertainties in the  $\text{N}_2$  flow (MFC) and water evaporation system. Combined uncertainties in pressure and water concentrations were  $\pm 0.77\%$  (for 1.5%  $\text{H}_2\text{O}$ ) and  $\pm 0.74\%$  (for 2%  $\text{H}_2\text{O}$ ). This means that absolute uncertainties in water concentrations in the  $\text{N}_2$  carry gas are  $(1.50 \pm 0.01)$  and  $(2.00 \pm 0.02)$  volume %. Temperature variations in the cell are negligible in the uncertainty calculations.

The composite absorption cross sections in 186.45–230.413 nm are calculated by calculating the mean cross-section data from the last three sequences and their respective standard deviations, which are taken to represent the  $1 - \sigma$  error assuming Gaussian statistics. The resulting cross sections are shown in Figure 1. The minimum measurable absorption in our experimental apparatus, calculated by the ratio of incident to detected light, is  $1.53 \times 10^{-4}$ , corresponding to a minimum measurable cross section of  $5.41 \times 10^{-25} \text{ cm}^2 \text{ molecule}^{-1}$ .

### 3.2. Comparison to Previous Data and Theoretical Expectations

In this section, we compare our measurements (Figure 1) to previously published data and theoretical expectations to assess their quality and ascertain our confidence in them.

Data to compare our measurements to are nonexistent for  $\lambda > 198 \text{ nm}$ ,<sup>17</sup> but some data sets are available for  $198 > \lambda > 190 \text{ nm}$  (Thompson et al. 1963; Cantrell et al. 1997; Chung et al. 2001; Parkinson & Yoshino 2003; Mota et al. 2005). Our data agree with the measurements of Thompson et al. (1963), Cantrell et al. (1997), and Chung et al. (2001), with best agreement with the data set of Chung et al. (2001), which is the most conservative of all data sets (i.e., presumes the lowest water absorption for wavelengths between 190 and 198 nm).

Our data agree with Mota et al. (2005) and Parkinson et al. (2003) at shorter wavelengths but disagree with these data sets at their red edges. At these red edges, both Mota et al. (2005) and Parkinson et al. (2003) show distinctive upturns in the water absorption at the long-wavelength edge of their

<sup>17</sup> A measurement at 207 nm was reported by Tan et al. (1978), but the measurements from this data set at  $>180 \text{ nm}$  are in tension by orders of magnitude with all other measurements and are considered to be erroneous (Chan et al. 1993); we therefore exclude it from consideration.



measurements, in disagreement with both the expected behavior of the spectra and Chung et al. (2001) and Thompson et al. (1963). There are many possible explanations for such disagreement between sets of data, including experimental limitations (i.e., most of the disagreements occur at the instrumental threshold of measurements), variation in baseline corrections, and other experimental setup concerns (e.g., whether equilibrium conditions in the system have been established before measurements, potential for underestimating water concentration, and scattering from H<sub>2</sub>O in their saturated measurements). Of these, experimental limitations are a particularly compelling explanation, since the disagreements with Mota et al. (2005) and Parkinson et al. (2003) occur where one would expect them to be a problem, i.e., where their H<sub>2</sub>O cross sections are weakest and their measurement setups are closest to their limits. We therefore attribute the upturn at the red edges of the data sets of Mota et al. (2005) and Parkinson et al. (2003) to experimental error; below, we apply this same logic to our own data set.

Theoretical predictions expect that, at room temperature, water absorbs very weakly at wavelengths  $\geq 180$  nm, losing intensity with a roughly exponential trend until it reaches the H–OH bond dissociation energy near 240 nm. This can be considered a vapor equivalent of Urbach’s rule, which predicts that, as an electronically excited band moves away from its peak, the absorption coefficient decreases approximately as an exponential of the transition frequency (Quickenden & Irvin 1980).

As wavelengths increase toward dissociation, the populations of the energy levels participating in the transitions that cause the spectral absorption become increasingly sparse. This thermal occupancy factor is the strongest effect in predicting absorption in this region and corresponds to an exponential decay of transition strength, which gives the cross section its recognizable log-linear shape between 180 and 240 nm. The opacity in this region is caused by transitions to excited electronic states of water, which are effectively unbound even at their lowest energy. Consequently, other weak effects can provide minor contributions toward the total absorption that can lead to a small upturn in the overall spectrum. For example, predissociation effects can broaden the wings of the hot, combination rovibronic bands in the region, resulting in a small gain in opacity. Additionally, Frank–Condon factors and Einstein-A coefficients, which are hard to predict in this region, can increase near dissociation and consequently limit the loss of line strength caused by the reduction in thermal occupancy of the transition states.

The new measured data presented here agree with the qualitative theoretical expectations of the spectral behavior of water in the wavelength range 186–215 nm. From 215 to 230 nm, our measured data exhibit an upward deviation from log-linear decrease, similar to the deviation reported in the long-wavelength edge of other previously measured data (e.g., Parkinson et al. 2003; Mota et al. 2005). This upward deviation in all three data sets corresponds to the region of the measurements that approaches the instrumental noise floor, which introduces uncertainty not only to each measured data point but also to the overall predicted absorption. It is therefore not fully certain that this upward deviation is physical.

Given the sensitivity of photochemical models to increased water absorption in the 186–230 nm region, we have adapted the measured cross sections presented here to minimize the possibility that our predicted water absorption is overestimated.

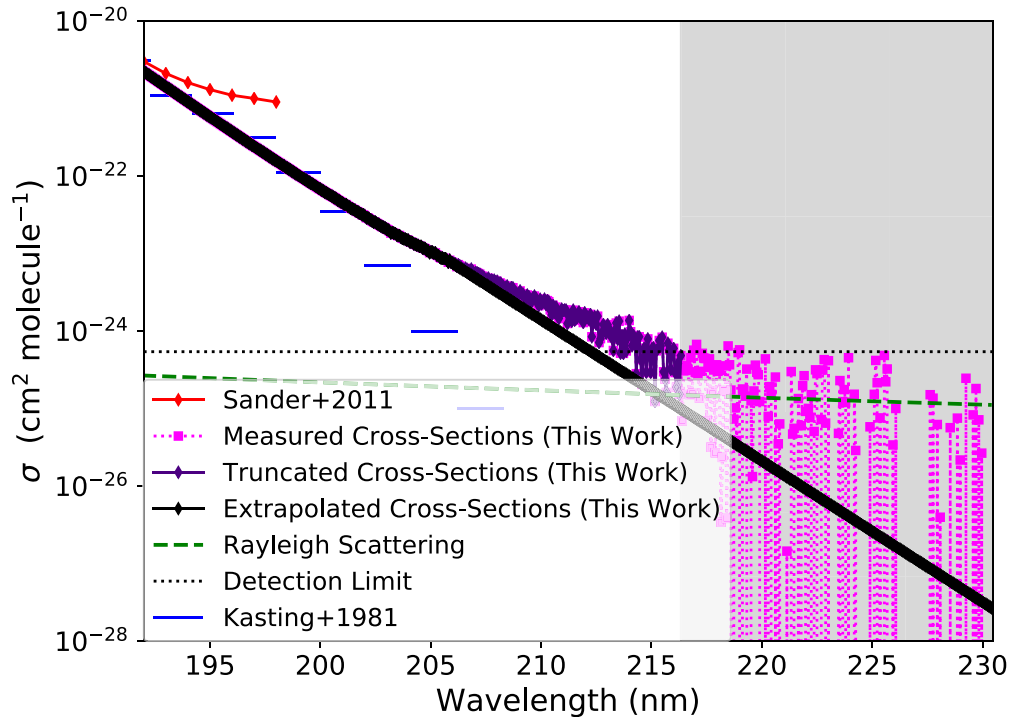
To this end, we considered two prescriptions for 292 K H<sub>2</sub>O(g) absorption cross sections for incorporation into our photochemical models. The first prescription corresponds to our measured data with a cutoff after 216.328 nm, which is where the ratio of the measured absorption to the errors first goes below 3. We term this the “cutoff” prescription. We note this is a conservative but unphysical prescription, since the water absorption at wavelengths above 216 nm is not expected to collapse but instead experience an exponential loss in intensity. Our second data set addresses the concerns above by replacing the measured data at wavelengths  $>205$  nm with a theoretical extrapolation, corresponding to a log-linear loss of absorption of our data from 186 to 205 nm toward dissociation (longer wavelengths). We term this the “extrapolation” prescription. This prescription is similar in spirit to that executed by Kasting & Walker (1981) but with the advantage of the greater spectral coverage and higher sensitivity of our new data set, which significantly affect the results. We note that this extrapolation is expected to underestimate overall opacity (see above for potential quantum chemical effects that can increase opacity near dissociation).

Figure 2 presents both of our prescriptions for 292 K NUV H<sub>2</sub>O(g) absorption cross sections; also shown are the prescription of Kasting & Walker (1981) and the recommended cross sections of Sander et al. (2011). At wavelengths  $<192$  nm, we employ the recommended cross sections of Sander et al. (2011; i.e., we replace the Parkinson et al. 2003 cross sections of Sander et al. 2011). Both prescriptions specified here should be considered conservative choices, in that if anything, they underestimate H<sub>2</sub>O(g) absorption in this wavelength range. Nevertheless, both prescriptions indicate H<sub>2</sub>O(g) absorption  $\geq 205$  nm to be orders of magnitude higher than previously considered, with profound photochemical implications (Section 5). Both prescriptions, together with the underlying measurements, are available at <https://github.com/sukritranjan/ranjanschwiertermanharman2020>.

#### 4. Model Intercomparison

We seek to determine the photochemical effects of our new H<sub>2</sub>O cross sections on the atmospheric composition of abiotic habitable worlds with anoxic CO<sub>2</sub>–N<sub>2</sub> atmospheres. However, modeling of these atmospheres is discordant, with disagreement on a broad range of topics. Broadly, the models feature order-of-magnitude disagreements as to the trace gas composition of such atmospheres, in particular their potential to accumulate photochemical CO and O<sub>2</sub> (Kasting 1990; Zahnle et al. 2008; Hu et al. 2012, 2020; Domagal-Goldman et al. 2014; Tian et al. 2014; Harman et al. 2015; Rimmer & Helling 2016; James & Hu 2018).

To resolve this disagreement and derive a robust model for use in this work, we intercompare the models of Hu et al. (2012), Harman et al. (2015), and ATMOS (Arney et al. 2016, commit #be0de64; *Archaeon+haze* template). For convenience, we allude to the model of Hu et al. (2012) as the “Hu model” and the model of Harman et al. (2015) as the “Kasting model” to reflect their primary developers, with the caveat that multiple workers have contributed to these models. We apply these models to the CO<sub>2</sub>-dominated benchmark planetary scenario outlined in Hu et al. (2012). This scenario corresponds to an abiotic rocky planet orbiting a Sun-like star with a 1 bar 90% CO<sub>2</sub>, 10% N<sub>2</sub> atmosphere with surface temperature 288 K. Appendices A and B present the details of the planetary scenario and boundary conditions adopted by these models. We focus on the surface mixing ratio of CO,  $r_{\text{CO}}$ , as the figure of



**Figure 2.** Cutoff and extrapolation prescriptions for the spectral absorption cross sections of 292K  $\text{H}_2\text{O}(\text{g})$ . Also shown are the recommended cross sections of Sander et al. (2011), the prescription of Kasting & Walker (1981), the Rayleigh scattering cross sections (Ranjan & Sasselov 2017), and the full data set of measured cross sections reported here. Our measured cross sections first dip below a  $3 - \sigma$  significance at 216.348 nm; in the spirit of conservatism, we consider our data at  $>216.348$  nm unreliable and demarcate it as such with gray shading. The dotted black line demarcates the detection limit of our apparatus (Section 3.1).

merit for the intercomparison. At the outset of the intercomparison, the predictions of  $[\text{CO}]$  for this planetary scenario varied by  $50\times$  between these models (Table C5).

We describe in detail the key differences between our models that drove the disagreement in  $r_{\text{CO}}$  in Appendix C. Briefly, we identified the following errors and necessary corrections in our models (see Appendix C, Table C1).

1. Correction of  $\text{CO}_2$  absorption cross sections. The Hu model approximated the NUV absorption cross sections of  $\text{CO}_2$  by its total extinction cross sections out to 270 nm. However, measurements indicate that for  $>201.58$  nm  $\text{CO}_2$ , extinction is scattering-dominated (Ityaksov et al. 2008), even though the reported bond dissociation energy of  $532.2 \pm 0.4 \text{ kJ mol}^{-1}$  (Darwent 1970) corresponds to 225 nm. In high- $\text{CO}_2$  scenarios, this error shielded  $\text{H}_2\text{O}$  from NUV photolysis, regardless of assumptions regarding  $\text{H}_2\text{O}$  NUV absorption. This led to underestimates of  $\text{H}_2\text{O}$  photolysis rates and  $[\text{OH}]$  and hence overestimates of  $[\text{CO}]$ ,  $[\text{O}]$ , and  $[\text{O}_2]$ . We corrected the  $\text{CO}_2$  cross sections in the Hu model to correspond to absorption (Ityaksov et al. 2008; Keller-Rudek et al. 2013).
2. Correction of reaction networks. We identified several errors in the reaction networks of the ATMOS and Kasting models. In the ATMOS model, these errors led  $\text{SO}_2$  to suppress  $\text{CO}$ , so that  $r_{\text{CO}}$  was low regardless of assumptions on NUV  $\text{H}_2\text{O}$  absorption. In the Kasting model, these errors did not affect the baseline scenario but led to  $\text{SO}_2$  suppression of  $\text{CO}$  in low-outgassing planetary scenarios. These errors and their suggested corrections are summarized in Appendix C, Table C2.
3. Self-consistent temperature–pressure profile. The temperature–pressure profile in the ATMOS Archaean

+haze scenario features a warm stratosphere due to shortwave stratospheric heating from high-altitude haze ultimately sourced from high-biogenic  $\text{CH}_4$  emission. This leads to a wet stratosphere and high  $\text{H}_2\text{O}$  photolysis rates. However, on a world lacking vigorous  $\text{CH}_4$  production (e.g., an abiotic world),  $[\text{CH}_4]$  is low, haze is not expected to form, and  $\text{CO}_2$ -rich anoxic atmospheres are expected to have had cold, dry stratospheres (DeWitt et al. 2009; Guzmán-Marmolejo et al. 2013; Arney et al. 2016). Therefore, when employing ATMOS Archaean +haze to this planet scenario, it is necessary to first calculate a consistent temperature–pressure profile.

We identified the following points of difference between our models.

1. Binary diffusion coefficient  $nD(X, Y)$ . Use of a generalized formulation (Equation (C3)) to estimate  $nD(X, Y)$ , relevant to diffusion-limited atmospheric escape, overestimates  $nD(\text{H}_2, \text{N}_2)$  and  $nD(\text{H}_2, \text{CO}_2)$  relative to laboratory measurements (Marrero & Mason 1972; Banks & Kockart 1973) and hence underestimates  $\text{pH}_2$  and  $r_{\text{CO}}$ . Surprisingly,  $nD(\text{H}, \text{CO}_2)$  has not yet been measured; we recommend this as a target for future laboratory studies.
2.  $\text{CO} + \text{OH}$  rate law. Prescriptions for the rate constant of the reaction  $\text{CO} + \text{OH} \rightarrow \text{CO}_2 + \text{H}$  have evolved significantly. Moving forward, we recommend the prescription of Burkholder et al. (2015), which is the most up-to-date known and is intermediate relative to the prescriptions incorporated into our models to date.
3.  $\text{CO} + \text{S} + \text{M}$  rate law. The reaction  $\text{CO} + \text{S} + \text{M} \rightarrow \text{OCS} + \text{M}$  has not been measured in the laboratory but has been invoked to explain Venusian OCS (Krasnopolsky 2007;

Yung et al. 2009). Assumption of this reaction modestly reduces  $r_{\text{CO}}$ . We identify this as a key reaction for laboratory follow-up; confirmation of this reaction mechanism will affirm our understanding of Venusian atmospheric chemistry, while refutation will signal a need to closely reexamine our photochemical models of Venus and Venus-like exoplanets.

If we repair these errors and align these parameters between our models, we find that our model predictions of  $r_{\text{CO}}$  agree to within a factor of 2, and that we can reproduce both the low ( $\sim 200$  ppm) and high ( $\sim 8200$  ppm) estimates for  $r_{\text{CO}}$  that have been reported in the literature (Appendix C.5; Appendix C, Table C3). The overwhelmingly dominant factor is the prescription adopted for the NUV absorption cross sections of  $\text{H}_2\text{O}(\text{g})$ . Prescriptions that omit this absorption (e.g., Sander et al. 2011) lead to high  $r_{\text{CO}}$ , and prescriptions that include this absorption (e.g., Kasting & Walker 1981) lead to low  $r_{\text{CO}}$ . The absorption measured in this work is higher in the NUV than considered by any of these prescriptions (Figure 2), implying  $r_{\text{CO}}$  to be lower than previously calculated by any model (Section 5). We conclude that we have resolved the disagreements between our models as measured by predictions of  $r_{\text{CO}}$ .

## 5. Updated Photochemical Model

We include our newly measured  $\text{H}_2\text{O}$  cross sections in the corrected Hu model using both the extrapolated and cutoff prescriptions detailed in Section 3.2. We verify that the model still reproduces the atmospheres of modern Earth and Mars as detailed in Hu et al. (2012). Table 1 presents the effects of the new  $\text{H}_2\text{O}$  cross sections on  $r_{\text{CO}}$  and  $r_{\text{O}_2}$  for the  $\text{CO}_2$ -dominated exoplanet scenario of Hu et al. (2012). For these calculations, we returned to the simulation parameters as originally prescribed by Hu et al. (2012), following the rationale given therein and to facilitate comparison with past results. In other words, we followed the simulation parameters tabulated in Table A1, not the uniform parameters adopted for the model intercomparison in Appendix C.5. For all model runs, we verified the maintenance of atmospheric redox balance (Hu et al. 2012).

### 5.1. Effect of New Cross Sections on $r_{\text{CO}}$ and $r_{\text{O}_2}$

The effects are dramatic: inclusion of the new  $\text{H}_2\text{O}$  cross sections, whether using the extrapolated or cutoff prescriptions, reduces  $r_{\text{CO}}$  by 2.5 orders of magnitude relative to the cross sections recommended by Sander et al. (2011; i.e., terminated at 198 nm) and 1 order of magnitude relative to the Kasting & Walker (1981) prescription to  $\sim 10$  ppm (Figure 3) for our abiotic  $\text{CO}_2$ - $\text{N}_2$  scenario. The new  $\text{H}_2\text{O}$  cross sections are larger and extend to longer wavelengths than the prescription of Kasting & Walker (1981), leading to  $\text{H}_2\text{O}$  photolysis rates that are  $\sim$ five times higher. These higher photolysis rates drive enhanced production of OH, especially at the bottom of the atmosphere where  $[\text{H}_2\text{O}]$  is highest (Figure 4), resulting in the efficient recombination of CO and O to  $\text{CO}_2$  via catalytic cycles ultimately triggered by  $\text{CO} + \text{OH} \rightarrow \text{CO}_2 + \text{H}$  (Harman et al. 2018). The new cross sections also drive enhanced production of H, visible as enhanced  $[\text{H}]$  in the bottom of the atmosphere.

Our  $\text{H}_2\text{O}$  absorption cross sections also negate the low-outgassing photochemical false-positive scenario for  $\text{O}_2$  on planets orbiting Sun-like stars. Specifically, it has been proposed that in the regime of lower outgassing of reductants

**Table 1**

Summary of Results from Corrected Model (i.e., with Corrected  $\text{CO}_2$  Cross Sections), with Results from Uncorrected Model Also Shown for Context

Parameters	$r_{\text{CO}}$	$r_{\text{O}_2}$	$J_{\text{H}_2\text{O}}$ ( $\text{cm}^{-2} \text{s}^{-1}$ )	$\Phi_{\text{Dep}}$ ( $\text{H cm}^{-2} \text{s}^{-1}$ )
<b>Standard Scenario</b>				
Uncorrected model	8.2E-3	1.5E-14	1.0E8	-4.2E9
Sander et al. (2011)	6.4E-3	9.2E-19	9.3E7	-3.7E9
$\text{H}_2\text{O}$				
Kasting & Walker (1981) $\text{H}_2\text{O}$	1.2E-4	9.5E-19	1.2E10	-2.0E10
Cutoff $\text{H}_2\text{O}$ (this work)	8.6E-6	7.2E-12	6.6E10	-6.0E10
Extrapolated $\text{H}_2\text{O}$ (this work)	1.3E-5	2.5E-12	5.3E10	-5.8E10
<b>Reduced Outgassing Scenarios</b>				
$\phi_{\text{H}_2} = 3 \times 10^9 \text{ cm}^{-2} \text{ s}^{-1}$				
Uncorrected model	1.2E-2	3.2E-6	3.0E7	-4.3E9
Sander et al. (2011)	9.5E-3	3.0E-6	2.9E7	-3.7E9
$\text{H}_2\text{O}$				
Extrapolated $\text{H}_2\text{O}$ (this work)	1.5E-5	2.8E-11	5.3E10	-8.5E9
$\phi_{\text{H}_2} = \phi_{\text{CH}_4} = 0 \text{ cm}^{-2} \text{ s}^{-1}$				
Uncorrected model	3.7E-2	1.5E-3	9.1E6	-1.8E9
Sander et al. (2011)	1.6E-2	2.1E-4	9.8E6	-1.8E9
$\text{H}_2\text{O}$				
Extrapolated $\text{H}_2\text{O}$ (this work)	1.6E-5	3.4E-11	5.3E10	-4.8E8

**Note.** The first subtable, titled ‘‘Standard Scenario,’’ illustrates the effect of different prescriptions for  $\text{H}_2\text{O}$  NUV absorption on CO and  $\text{O}_2$  concentrations in our standard scenario (Table B1). The second subtable, titled ‘‘Reduced Outgassing Scenarios,’’ illustrates the effect of our new cross sections on the abiotic  $\text{O}_2$  buildup scenario reported in Hu et al. (2012). The enhanced  $\text{H}_2\text{O}$  photolysis efficiently recombines CO and  $\text{O}_2$  and removes this abiotic false-positive scenario for  $\text{O}_2$ . In this table,  $r_X$  is the surface mixing ratio of X (relative to dry  $\text{CO}_2 + \text{N}_2$ ),  $J_{\text{H}_2\text{O}}$  is the column-integrated photolysis rate, and  $\Phi_{\text{Dep}}$  is the net flux of reducing power out of the ocean, in H-equivalents, relevant to the question of global redox balance ( $\Phi_{\text{Dep}} < 0 \Rightarrow$  reducing power enters the ocean).

( $\text{H}_2$ ,  $\text{CH}_4$ ),  $\text{O}_2$  sourced from  $\text{CO}_2$  photolysis can accumulate to detectable, near-biotic levels on planets orbiting solar-type stars. This constitutes a potential false-positive scenario for  $\text{O}_2$  as a biosignature gas (Hu et al. 2012; Harman et al. 2015; James & Hu 2018). With our new  $\text{H}_2\text{O}$  cross sections, we find that photolytic OH efficiently recombines CO and O even in the absence of  $\text{CH}_4$  and  $\text{H}_2$  outgassing (Figure 5). Interestingly, though we find very low  $\text{H}_2$  and  $\text{CH}_4$  in the low-outgassing case, we nonetheless report higher  $p\text{H}_2$  and  $p\text{CH}_4$  compared to Hu et al. (2012). We speculate H sourced from  $\text{H}_2\text{O}$  photolysis to support the  $\text{CH}_4$  and  $\text{H}_2$ .

### 5.2. Effect of New Cross Sections on Other Atmospheric Gases

A powerful oxidizing agent, OH efficiently reacts with a broad range of reduced species (e.g., Catling & Kasting 2017). It is consequently unsurprising to find that the enhancement in OH production from our larger  $\text{H}_2\text{O}$  cross sections leads to suppression of a broad range of the trace compounds present in anoxic atmospheres, including  $\text{H}_2\text{S}$ ,  $\text{SO}_2$ , and  $\text{S}_8$  aerosol (Figure 3).

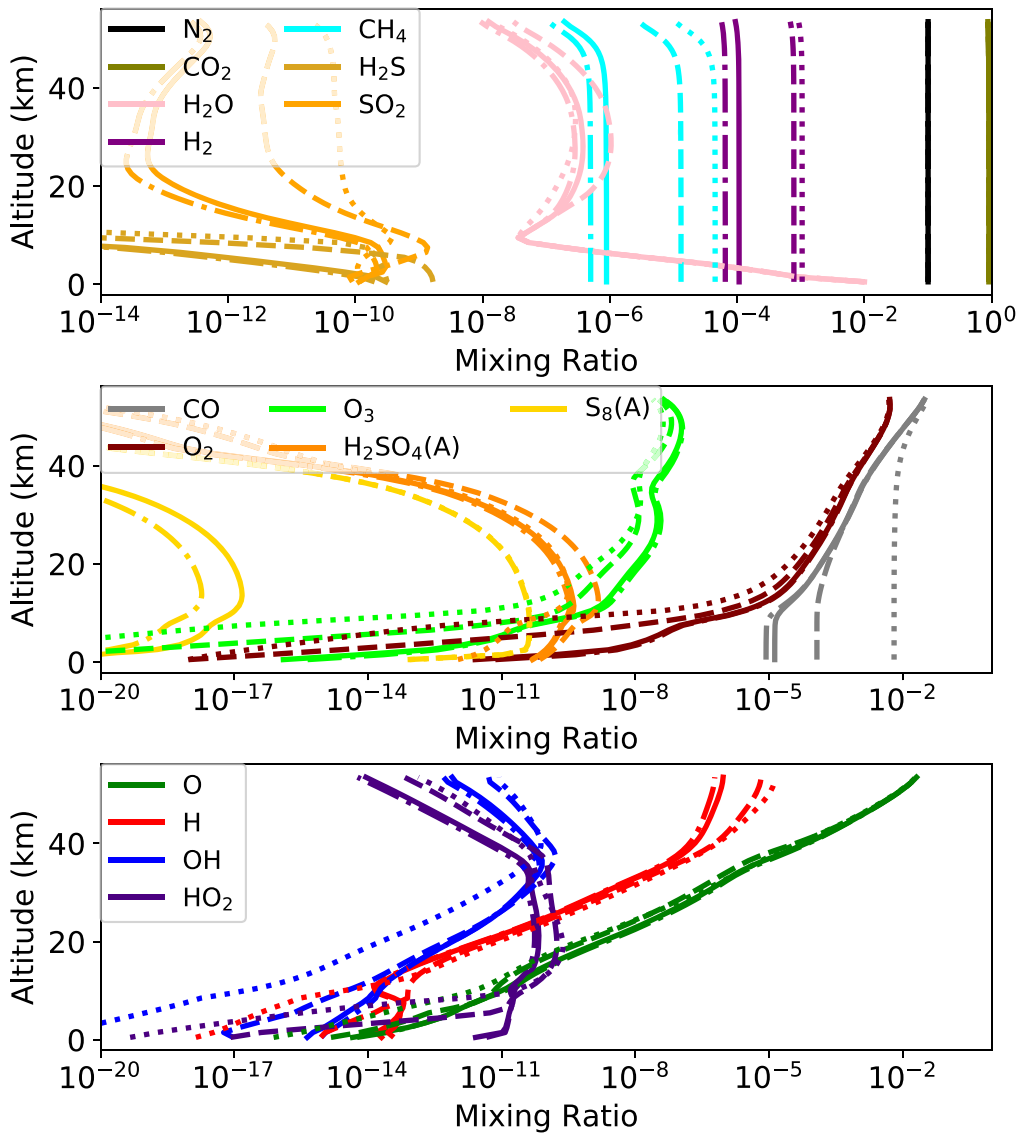


**Figure 3.** Mixing ratio (relative to dry  $\text{CO}_2/\text{N}_2$ ) as a function of altitude for outgassed species (top), photochemical by-products (middle), and radicals (bottom). These predictions were derived from the Hu model, with corrected  $\text{CO}_2$  cross sections. The line types demarcate different prescriptions regarding the  $\text{H}_2\text{O}$  cross sections. Specifically, the solid lines refer to the “extrapolation” prescription proposed here; the dashed-dotted lines, the “cutoff” prescription; the dashed lines, the Kasting & Walker (1981) prescription; and the dotted lines, the Sander et al. (2011) prescription. The higher  $\text{H}_2\text{O}$  absorption we propose here leads to higher  $[\text{OH}]$  and  $[\text{H}]$  and concomitantly lower  $[\text{CO}]$ ,  $[\text{CH}_4]$ , and  $[\text{H}_2]$ .

Perhaps most dramatic is the suppression of  $\text{CH}_4$ . With our new  $\text{H}_2\text{O}$  cross sections, we predict the concentration of volcanically outgassed  $\text{CH}_4$  to be 2 orders of magnitude lower than using the Sander et al. (2011) cross sections and 1.5 orders of magnitude lower than using the Kasting & Walker (1981) cross sections. We predict the main sink on  $\text{CH}_4$  to be  $\text{OH}$  via the reaction  $\text{OH} + \text{CH}_4 \rightarrow \text{CH}_3 + \text{H}_2\text{O}$ , consistent with previous work (e.g., Rugheimer & Kaltenecker 2018). This suppression of  $\text{CH}_4$  is significant because  $\text{CH}_4$  is spectrally active and has been proposed as a potentially detectable component of exoplanet atmospheres and a probe of planetary processes, including life (Guzmán-Marmolejo et al. 2013; Krissansen-Totton et al. 2018; Rugheimer & Kaltenecker 2018). Our work suggests it may be harder to detect this gas in anoxic atmospheres than previously considered.

Also key is our finding of photochemical suppression of  $\text{H}_2$  (but see caveat below). Prior simulations concluded that the

main sink for  $\text{H}_2$  on anoxic terrestrial planets (e.g., early Earth) was escape to space and that  $p\text{H}_2$  was to first order set by the balance between  $\text{H}_2$  outgassing and (diffusion-limited) escape (Kasting 1993, 2014). Indeed, under the assumption of the Kasting & Walker (1981) cross sections, we recover this result ourselves. However, with our new cross sections, we find the sink due to the reaction  $\text{H}_2 + \text{OH} \rightarrow \text{H}_2\text{O} + \text{H}$  to be the dominant sink for  $\text{H}_2$ , which suppresses  $p\text{H}_2$  by 1 order of magnitude relative to past predictions. This reaction converts relatively unreactive  $\text{H}_2$  to relatively reactive  $\text{H}$ , which can undergo further reactions to ultimately be deposited onto the surface in the form of more-soluble reduced chemical species. This is reflected in the enhanced transfer of reductants from the atmosphere to the oceans calculated by our model (Table 1), in which essentially all of the reducing power outgassed as  $\text{H}_2$  is returned to the surface, primarily via rainout. This suggests more efficient delivery of reduced organic compounds from the



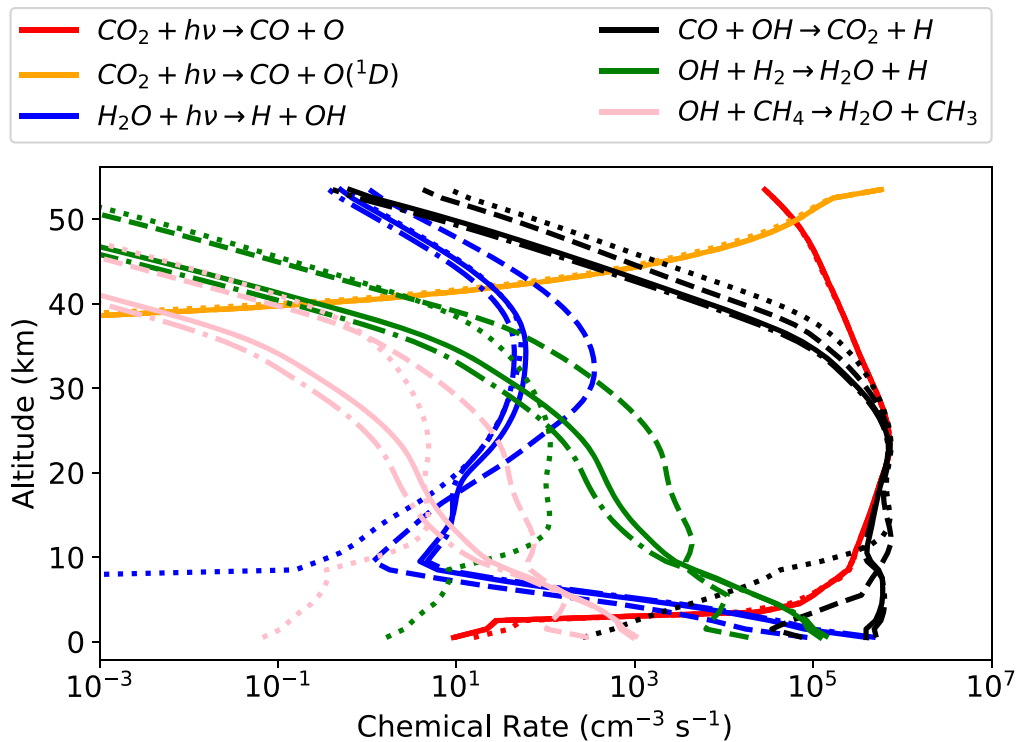


**Figure 4.** Key reaction rates as a function of altitude. These predictions were derived from the Hu model, with corrected  $\text{CO}_2$  cross sections. The line types demarcate different prescriptions regarding the  $\text{H}_2\text{O}$  cross sections. Specifically, the solid lines refer to the “extrapolation” prescription proposed here; the dashed-dotted lines, the “cutoff” prescription; the dashed lines, the Kasting & Walker (1981) prescription; and the dotted lines, the Sander et al. (2011) prescription. The higher  $\text{H}_2\text{O}$  absorption we propose here dramatically enhances  $\text{OH}$  and  $\text{H}$  production from  $\text{H}_2\text{O}$  photolysis, especially in the bottom of the atmosphere, leading to much lower  $\text{CO}$ ,  $\text{CH}_4$ , and  $\text{H}_2$  due to suppression by  $\text{OH}$ .

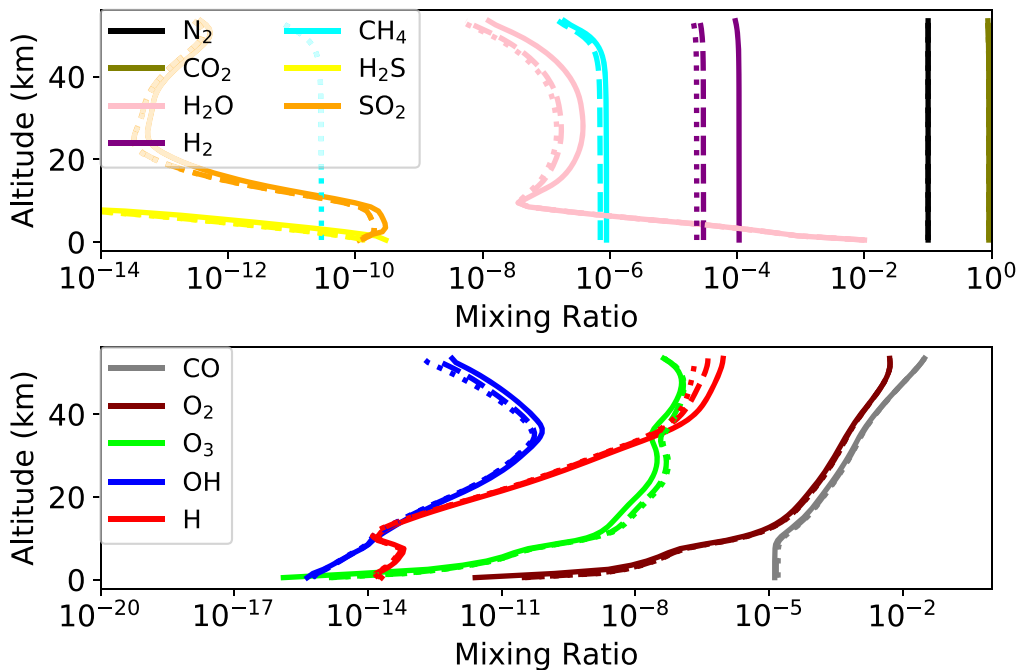


**Figure 5.** Mixing ratio (relative to dry  $\text{CO}_2/\text{N}_2$ ) as a function of altitude for outgassed species (top) and photochemical by-products (bottom), calculated with the corrected Hu model and the extrapolation prescription for  $\text{H}_2\text{O}$  absorption. The solid lines assume full outgassing ( $\phi_{\text{H}_2} = 3 \times 10^{10}$ ,  $\phi_{\text{CH}_4} = 3 \times 10^8 \text{ cm}^{-2} \text{ s}^{-1}$ ); the dashed lines, reduced outgassing ( $\phi_{\text{H}_2} = 3 \times 10^9$ ,  $\phi_{\text{CH}_4} = 3 \times 10^8 \text{ cm}^{-2} \text{ s}^{-1}$ ); and the dotted lines, no outgassing of  $\text{H}_2$  and  $\text{CH}_4$  ( $\phi_{\text{H}_2} = 0 \text{ cm}^{-2} \text{ s}^{-1}$ ). The higher  $\text{H}_2\text{O}$  absorption we measure obviates the low-outgassing false photochemical false-positive mechanism for  $\text{O}_2$ .

atmosphere, of relevance to origin-of-life studies (e.g., Cleaves 2008; Harman et al. 2013; Rimmer & Rugheimer 2019).

The above results were derived without assuming global redox balance (Kasting 2013; Tian et al. 2014; Harman et al. 2015; James & Hu 2018). The principle of global redox

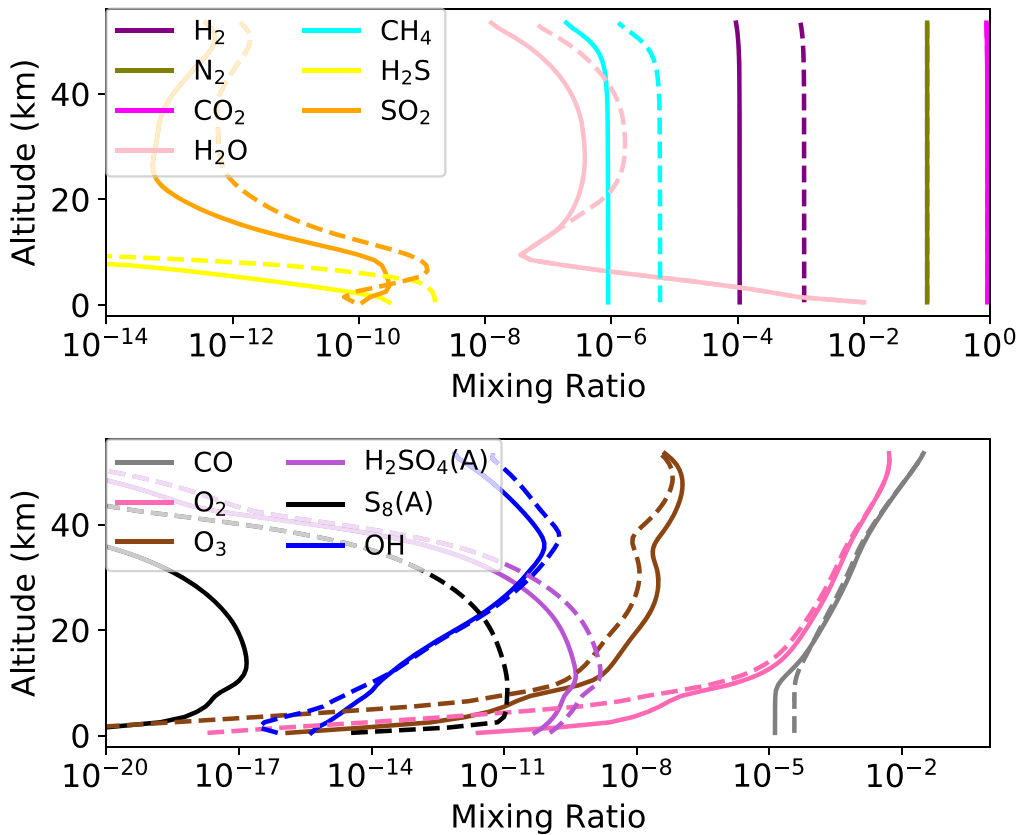


**Figure 6.** Mixing ratio (relative to dry CO<sub>2</sub>/N<sub>2</sub>) as a function of altitude for outgassed species (top) and photochemical by-products (bottom), calculated with the corrected Hu model and the extrapolation prescription for H<sub>2</sub>O absorption. The solid lines were calculated without assuming global redox balance; the dashed lines assumed global redox balance. Redox balance makes the atmosphere more reducing, stabilizing reduced species.

balance is based on the observation that the main mechanisms by which we know free electrons to be added or removed from the ocean–atmosphere system on Earth are oxidative weathering and biologically mediated burial of reductants. The former is not relevant to anoxic atmospheres; the latter is not relevant to abiotic worlds. If one zeros these terms in the atmosphere–ocean redox budgets, one finds that in steady state, any supply of reductants or oxidants to the planet surface should be counterbalanced by return flux to or deposition from the atmosphere (Harman et al. 2015). This is practically implemented in models by prescribing an oceanic H<sub>2</sub> return flux in the case where reductants are net deposited into the ocean by the atmosphere (mostly by rainout) or an increased H<sub>2</sub> deposition velocity in the (uncommon) case where oxidants are net deposited (Tian et al. 2014; Harman et al. 2015; James & Hu 2018). Figure 6 presents the effects of requiring global redox balance. We find a return H<sub>2</sub> flux of  $4.4 \times 10^{10} \text{ cm}^{-2} \text{ s}^{-1}$ , a return of pH<sub>2</sub> to the escape-limited  $1 \times 10^{-3}$  bars, and an increase in CH<sub>4</sub> by 1 order of magnitude ( $2 \times$  lower than when assuming the Kasting & Walker 1981 cross sections). Overall, we predict pH<sub>2</sub> and pCH<sub>4</sub> to be significantly higher on worlds obeying global redox balance, as has been proposed for abiotic worlds.

Our calculations highlight the importance of the question of global redox balance for abiotic planets. In the past, it has been possible to largely ignore this question in conventional planetary scenarios because the deposition terms in the redox budget have been relatively small. However, our new cross sections suggest that the processing of H<sub>2</sub> into soluble reductants is efficient, the deposition terms are large, and the

assumption of global redox balance has a significant impact on the buildup of spectrally active, potentially detectable species in conventional planetary scenarios.

Whether abiotic anoxic planets are in global redox balance requires careful consideration. The theory of global redox balance rests on the assumption that biological mediation is required for burial of reductants. Biologically mediated burial is the dominant mode on modern Earth (Walker 1974). However, to our knowledge, it is not yet determined whether biotic burial is the *only* possible mode of reductant burial. We may draw an analogy to the theory of abiotic nitrogen fixation, where it was long assumed that on abiotic worlds (e.g., prebiotic Earth), lightning-fixed nitrogen could accumulate almost indefinitely in the ocean as nitrate/nitrite (NO<sub>3</sub><sup>-</sup>), since the today-dominant biological sinks of NO<sub>3</sub><sup>-</sup> were absent (e.g., Mancinelli & McKay 1988; Wong et al. 2017; Hu & Diaz 2019). However, there exist abiotic sinks on NO<sub>3</sub><sup>-</sup>, slower than the biotic sinks but still important on geological timescales; these sinks suppress oceanic [NO<sub>3</sub><sup>-</sup>] and stabilize atmospheric N<sub>2</sub> (Ranjan et al. 2019). Similarly, there may exist abiotic reductant/oxidant burial mechanisms that are relevant on geological timescales (e.g., Fe<sup>2+</sup> photooxidation, Kasting et al. 1984; magnetite burial, James & Hu 2018); the existence of such mechanisms should be explored further. Alternately, Mars may provide a touchstone. Like Earth, early Mars should have hosted an abiotic ocean under an anoxic atmosphere, but unlike Earth, the lack of tectonic activity and hydrology means that geological evidence from this epoch may be preserved (Citron et al. 2018; Sasselov et al. 2020). Are there geological fingerprints of the presence or absence of redox balance (e.g.,

evidence of widespread abiotic reductant burial) that future missions might detect? If so, such measurements could bound the relevant parameter space for the global redox balance hypothesis.

## 6. Discussion and Conclusions

We present the first measurements of  $\text{H}_2\text{O}$  cross sections in the NUV ( $>200\text{ nm}$ ) at habitable temperatures ( $T = 292\text{ K} < 373\text{ K}$ ) and show them to be far higher than assumed by previous prescriptions. These cross sections are critical because in anoxic atmospheres, the atmosphere is transparent at these wavelengths, and water can efficiently photolyze down to the surface (Harman et al. 2015; Ranjan & Sasselov 2017). In anoxic atmospheres, this  $\text{H}_2\text{O}$  photolysis is the ultimate source of atmospheric OH, a key control on atmospheric chemistry in general and CO in particular.

To assess the photochemical impact of these new cross sections on atmospheric composition, we apply a photochemical model to a planetary scenario corresponding to an abiotic habitable planet with an anoxic,  $\text{CO}_2\text{-N}_2$  atmosphere orbiting a Sun-like star. This planet scenario is representative of early (prebiotic) Earth, Mars, and Venus and analogous exoplanets. Model predictions of the atmospheric composition of such worlds are highly divergent in the literature; through a model intercomparison, we have identified the errors and divergent assumptions driving these differences and reconciled our models.

Incorporating these newly measured cross sections into our corrected model enhances OH production and suppresses  $r_{\text{CO}}$  by 1–2.5 orders of magnitude relative to past calculations. This implies less CO on early Earth for prebiotic chemistry and primitive ecosystems (Kasting 2014), suggesting the need to consider alternate reductants. It also implies that CO will be a more challenging observational target for rocky exoplanet observations than we might previously have hoped. However, if surface production of CO from processes like impacts, volcanism, or biology (Kasting 2014; Schwieterman et al. 2019; Wogan & Catling 2020) is sufficient to saturate the enhanced OH sink due to more efficient  $\text{H}_2\text{O}$  photolysis, CO may yet enter runaway and build to potentially detectable concentrations; we plan further investigation. On the other hand, the more efficient OH-catalyzed recombination of CO and O also removes the proposed low-outgassing false-positive mechanism for  $\text{O}_2$  (Hu et al. 2012). This reduces (but does not completely obviate; Wordsworth & Pierrehumbert 2014) the potential ambiguities regarding  $\text{O}_2$  as a biosignature for planets orbiting Sun-like stars.

The situation on planets orbiting lower-mass stars, e.g., M dwarfs, may be different. These cooler stars are dimmer in the NUV compared to Sun-like stars, meaning we expect the effect of our enhanced NUV  $\text{H}_2\text{O}$  cross sections to be muted (Segura et al. 2005; Ranjan et al. 2017a). On these planets, higher  $r_{\text{CO}}$  and  $r_{\text{O}_2}$  may be possible (Schwieterman et al. 2019; Hu et al. 2020); we plan further study. Further, these results do not impact  $\text{O}_2$ -rich planets analogous to the modern Earth, since in these atmospheres, direct  $\text{H}_2\text{O}$  photolysis is a minor contributor to OH production.

In addition to CO,  $\text{H}_2\text{O}$ -derived OH can suppress a broad range of species in anoxic atmospheres. In particular, the larger  $\text{H}_2\text{O}$  cross sections we measure in this work lead to substantial enhancements in OH attack on  $\text{H}_2$  and  $\text{CH}_4$ , suppressing these

gases in the abiotic scenario by 1–2 orders of magnitude relative to past calculations and suggesting that spectroscopic detection of  $\text{CH}_4$  on anoxic exoplanets will be substantially more challenging than previously considered (Reinhard et al. 2017; Krissansen-Totton et al. 2018). However, this finding is sensitive to assumptions of global redox balance. If reductants cannot be removed from the ocean by burial, as has been proposed for abiotic planets, then the return flux of reductants from the ocean (parameterized as  $\text{H}_2$ ) compensates for much of the  $\text{CH}_4$  and all of the  $\text{H}_2$  suppression. Regardless, rainout of reductants to the surface is enhanced, which is relevant to prebiotic chemistry (see Benner et al. 2019).

In prior calculations, enforcement of global redox balance resulted in relatively small changes in many planetary scenarios, including the scenario studied here. With the enhanced OH production driven by our higher  $\text{H}_2\text{O}$  cross sections, this is no longer the case. This sensitivity to the assumption of global redox balance highlights the need to carefully consider the global redox balance hypothesis and, in particular, its key premise that abiotic reductant burial is always geologically insignificant. Early Mars may provide a test case for the theory of redox balance, in that it may have hosted an abiotic ocean underlying an anoxic atmosphere early in its history, and geological remnants of this era might persist due to the lack of hydrologic and tectonic activity since 3.5 Ga. If abiotic reductant burial produces a detectable geological signature, then future missions can search for that signature, directly testing the global redox balance hypothesis. Further work to consider processes and signatures of abiotic reductant burial is required.

In this paper, we have focused on an abiotic planet scenario. We note that all of our specific findings (e.g., very low  $r_{\text{CO}}$ ) may not generalize to biotic scenarios. Biological production or uptake of gases may significantly outpace photochemical sources and sinks; for example, if biological CO production can outpace photolytic OH supply, then CO may nonetheless build to high, potentially detectable concentrations (Schwieterman et al. 2019). Detailed case-by-case modeling of biotic scenarios is required. However, our general point that OH production is higher than previously considered on anoxic habitable planets applies to biotic worlds as well, implying that spectrally active trace gases have a higher bar to clear to build to high concentrations than previously considered.

In this work, we have ignored nitrogenous chemistry, in particular the  $\text{NO}_x$  catalytic chemistry triggered by lightning-generated NO (Ardaseva et al. 2017; Harman et al. 2018). We justify this exclusion on the basis that this chemistry is most important when CO is high (Kasting 1990), and our models indicate that CO is photochemically suppressed. We conducted a sensitivity test to the inclusion of NO-triggered nitrogenous chemistry with the Kasting model and found a negligible (percent-level) impact on  $r_{\text{CO}}$ . Note that nitrogenous chemistry has been proposed to play a more dominant role on M dwarf planets (Hu et al. 2020); for such worlds, this chemistry must be included.

Our work highlights the critical need for laboratory measurements and/or theoretical calculations of the inputs to photochemical models. We show the sensitivity of the models to  $\text{H}_2\text{O}$  NUV cross sections; we recommend further characterization of these cross sections, both to confirm our own results and to extend these cross sections, e.g., to longer wavelengths

and lower temperatures. In particular, we reiterate that our prescriptions for H<sub>2</sub>O NUV cross sections are conservative, and the true absorption may be yet higher; higher S/N measurements at longer wavelengths are required to rule on this possibility. Further, our 292 K cross sections are good proxies for H<sub>2</sub>O absorption on temperate terrestrial planets because the nonlinear decrease in H<sub>2</sub>O saturation pressure with temperature means that most H<sub>2</sub>O is confined to the temperate lower atmosphere. However, on cold planets (e.g., modern Mars), the lower atmosphere is also cold, meaning use of 292 K cross sections may overestimate the H<sub>2</sub>O opacity and photolysis rate.<sup>18</sup> Similarly, we have here assumed a photolysis quantum efficiency of unity, i.e., that absorption of each  $\leq 230$  nm photon leads to H<sub>2</sub>O photolysis. If this assumption is incorrect, then the true photolysis rate will be lower than we have modeled here.

Finally, some of the reactions encoded into our models and/or their reaction rate constants are assumed or disputed; these reactions should be experimentally or theoretically characterized to confirm or refute these assumptions. In particular, we identify the reactions  $\text{CO} + \text{S} + \text{M} \rightarrow \text{OCS} + \text{M}$ ,  $\text{HO}_2 + \text{SO}_2 \rightarrow \text{OH} + \text{SO}_3$ ,  $\text{HO}_2 + \text{SO}_2 \rightarrow \text{O}_2 + \text{HSO}_2$ ,  $\text{SO} + \text{HO}_2 \rightarrow \text{SO}_2 + \text{OH}$ ,  $\text{SO} + \text{HO}_2 \rightarrow \text{SO}_2 + \text{OH}$ ,  $\text{SO} + \text{HO}_2 \rightarrow \text{O}_2 + \text{HSO}$ , and  $\text{N} + \text{O}_3 \rightarrow \text{NO} + \text{O}_2$  as targets for further investigation (Graham et al. 1979; Yung & Demore 1982; Wang & Hou 2005; Yung et al. 2009; Burkholder et al. 2015).

We thank Iouli Gordon, Eamon Conway, Robert Hargreaves, Mike Wong, Kevin Zahnle, Timothy Lee, Shawn Domagal-Goldman, Mark Claire, David Catling, Nick Wogan, and Jim Kasting for helpful discussions and answers to questions. We thank an anonymous reviewer for critical feedback that improved this work. This work was supported in part by a grant from the Simons Foundation (SCOL grant 495062 to S.R.) and the Heising-Simons Foundation (51 Pegasi b Fellowship to C.S.S.). E.W.S. gratefully acknowledges support by NASA Exobiology grant 18-EXO18-0005 and NASA Astrobiology Program grants NNA15BB03A and 80NSSC18K0829. The work has received funding partly from the EMPIR program cofinanced by the Participating States and from the European Union’s Horizon 2020 research and innovation program (Grant Number 16ENV08). This research has made use of NASA’s Astrophysics Data System and the MPI-Mainz UV-VIS Spectral Atlas of Gaseous Molecules (Keller-Rudek et al. 2013).

## Appendix A

### Detailed Simulation Parameters for Planetary Scenario

In Table A1, we present the simulation parameters of our models for the CO<sub>2</sub>-dominated planet scenario we consider. To make our models agree, we must implement the corrections summarized in Table C1 and adjust our models to use common inputs and formalisms as summarized in Table C4.

**Table A1**  
Simulation Parameters for Planetary Scenario

Scenario Parameter	Hu	ATMOS	Kasting
Model	Hu et al. (2012)	Arney et al. (2016)	Harman et al. (2015)
Reaction network	As in Hu et al. (2012) (Excludes N-, C <sub>&gt;2</sub> -chem)	Archean scenario	As in Harman et al. (2015)
Stellar type	Sun	Sun	Sun
Semimajor axis		1.3 au	
Planet size		1 $M_{\oplus}$ , 1 $R_{\oplus}$	
Surface albedo	0.	0.25	0.25
Major atmospheric components		0.9 bar CO <sub>2</sub> , 0.1 bar N <sub>2</sub> <sup>a</sup>	
Surface temperature ( $z = 0$ km)		288 K	
Surface $r_{\text{H}_2\text{O}}$ (lowest atmospheric bin)		0.01	
Eddy diffusion profile		See Figure C3	
Temperature–pressure profile		See Figure C3	
Vertical resolution	0–54 km, 1 km steps	0–100 km, 0.5 km steps	0–100 km, 1 km steps
Rainout	Earth-like; rainout turned off for H <sub>2</sub> , CO, CH <sub>4</sub> , NH <sub>3</sub> , N <sub>2</sub> , C <sub>2</sub> H <sub>2</sub> , C <sub>2</sub> H <sub>4</sub> , C <sub>2</sub> H <sub>6</sub> , and O <sub>2</sub> to simulate saturated ocean on abiotic planet	Earth-like (all species)	Earth-like (all species)
Lightning		Off	
Global redox conservation	No	No	Yes

#### Note.

<sup>a</sup> In the Hu model, pN<sub>2</sub> is fixed. In the ATMOS and Kasting models, pN<sub>2</sub> is adjusted to maintain dry  $P = 1$  bar. Photochemical and outgassed products do not build to levels comparable to the N<sub>2</sub> inventory in the scenario simulated here; consequently, this difference does not affect our results.

<sup>18</sup> At lower temperatures, fewer energy levels can be populated, which decreases the total number of active transition frequencies and subsequent cross-sectional opacity (see, for example, Schulz et al. 2002).



## Appendix B

### Detailed Boundary Conditions for Planetary Scenario

In this appendix, we present the species used in each of our models and their corresponding boundary conditions used in our initial model reconciliation (Table B1). For all species, we assign either a fixed surface mixing ratio or a surface flux. The only species assigned fixed surface mixing ratios are CO<sub>2</sub>, N<sub>2</sub>, and H<sub>2</sub>O (for rationale, see Hu et al. 2012). For species with a surface flux, the species is assumed to be injected in the bottommost layer of the atmosphere, i.e., PARAMNAME = 1 in ATMOS. It is assumed that H and H<sub>2</sub> escape at their diffusion-limited rates; for all other species, the escape/delivery flux is prescribed as zero.

While our models generally assume the same major species and many of the same minor species, there are some key

differences driven primarily by different assumptions regarding reaction network; they are given as follows.

1. The Kasting model does not include polysulfur species. This is because the polymerization of elemental sulfur to form an S<sub>8</sub> aerosol is ignored on the basis that this is a minor exit for S in this relatively oxidized atmospheric scenario; instead, S is assigned a high deposition velocity of 1 cm s<sup>-1</sup>.
2. The Hu model excludes all nitrogenous species other than N<sub>2</sub>. This is because the chosen boundary conditions precluded reactive N (no lightning, no thermospheric N), meaning they could neglect N chemistry.

In the planetary scenario considered here, these differences do not significantly affect  $r_{\text{CO}}$ , and we ignore them for the purposes of this model intercomparison.

**Table B1**  
Species Choice and Treatment for the Photochemical Models Used in This Study

Species	Hu	Type ATMOS	Kasting	Surface Flux (cm <sup>-2</sup> s <sup>-1</sup> )	Surface Mixing Ratio (Relative to CO <sub>2</sub> +N <sub>2</sub> )	Dry Deposition Velocity (cm s <sup>-1</sup> )	TOA Flux (cm <sup>-2</sup> s <sup>-1</sup> )
H	X	X	X	0	–	1	Diffusion-limited
H <sub>2</sub>	X	X	X	$3 \times 10^{10}$	–	0	Diffusion-limited
O	X	X	X	0	–	1	0
O(1D)	X	F	F	0	–	0	0
O <sub>2</sub>	X	X	X	0	–	0	0
O <sub>3</sub>	X	X	F	0	–	0.4	0
OH	X	X	X	0	–	1	0
HO <sub>2</sub>	X	X	X	0	–	1	0
H <sub>2</sub> O	X	X	X	–	0.01	0	0
H <sub>2</sub> O <sub>2</sub>	X	X	X	0	–	0.5	0
CO <sub>2</sub>	X	C	X	–	0.9	0	0
CO	X	X	X	0	–	$1 \times 10^{-8}$	0
CH <sub>2</sub> O	X	...	X	0	–	0.1	0
CHO	X	...	X	0	–	0.1	0
C	X	...	...	0	–	0	0
CH	X	X	...	0	–	0	0
CH <sub>2</sub>	X	...	...	0	–	0	0
<sup>1</sup> CH <sub>2</sub>	X	F	F	0	–	0	0
<sup>3</sup> CH <sub>2</sub>	X	X	F	0	–	0	0
CH <sub>3</sub>	X	X	X	0	–	0	0
CH <sub>4</sub>	X	X	X	$3 \times 10^8$	–	0	0
CH <sub>3</sub> O	X	X	F	0	–	0.1	0
CH <sub>4</sub> O	X	...	...	0	–	0.1	0
CHO <sub>2</sub>	X	...	...	0	–	0.1	0
CH <sub>2</sub> O <sub>2</sub>	X	...	...	0	–	0.1	0
CH <sub>3</sub> O <sub>2</sub>	X	X	F	0	–	0	0
CH <sub>4</sub> O <sub>2</sub>	X	...	...	0	–	0.1	0
C <sub>2</sub>	X	X	...	0	–	0	0
C <sub>2</sub> H	X	X	...	0	–	0	0
C <sub>2</sub> H <sub>2</sub>	X	X	...	0	–	0	0
C <sub>2</sub> H <sub>3</sub>	X	X	...	0	–	0	0
C <sub>2</sub> H <sub>4</sub>	X	X	...	0	–	0	0
C <sub>2</sub> H <sub>5</sub>	X	X	F	0	–	0	0
C <sub>2</sub> H <sub>6</sub>	X	X	X	0	–	$1 \times 10^{-5}$	0
C <sub>2</sub> HO	X	...	...	0	–	0	0
C <sub>2</sub> H <sub>2</sub> O	X	...	...	0	–	0.1	0
C <sub>2</sub> H <sub>3</sub> O	X	...	F	0	–	0.1	0
C <sub>2</sub> H <sub>4</sub> O	X	...	...	0	–	0.1	0
C <sub>2</sub> H <sub>5</sub> O	X	...	...	0	–	0.1	0
S	X	X	...	0	–	0	0
S <sub>2</sub>	X	X	...	0	–	0	0
S <sub>3</sub>	X	F	...	0	–	0	0
S <sub>4</sub>	X	F	...	0	–	0	0
SO	X	X	X	0	–	0	0
SO <sub>2</sub>	X	X	X	$3 \times 10^9$	–	1	0
<sup>1</sup> SO <sub>2</sub>	X	F	F	0	–	0	0
<sup>3</sup> SO <sub>2</sub>	X	F	F	0	–	0	0
H <sub>2</sub> S	X	X	X	$3 \times 10^8$	–	0.015	0
HS	X	X	X	0	–	0	0
HSO	X	X	X	0	–	0	0

**Table B1**  
(Continued)

Species	Hu	Type ATMOS	Kasting	Surface Flux ( $\text{cm}^{-2} \text{s}^{-1}$ )	Surface Mixing Ratio (Relative to $\text{CO}_2+\text{N}_2$ )	Dry Deposition Velocity ( $\text{cm s}^{-1}$ )	TOA Flux ( $\text{cm}^{-2} \text{s}^{-1}$ )
$\text{HSO}_2$	X	...	...	0	–	0	0
$\text{HSO}_3$	X	F	F	0	–	0.1	0
$\text{HSO}_4$	X	X	X	0	–	1	0
$\text{H}_2\text{SO}_4(\text{A})$	A	A	A	0	–	0.2	0
$\text{S}_8$	X	...	...	0	–	0	0
$\text{S}_8(\text{A})$	A	A	...	0	–	0.2	0
$\text{N}_2$	C	C	C	–	0.1	0	0
OCS	X	X	...	0	–	0.01	0
CS	X	X	...	0	–	0.01	0
$\text{CH}_3\text{S}$	X	...	...	0	–	0.01	0
$\text{CH}_4\text{S}$	X	...	...	0	–	0.01	0

**Note.** (1) For species type, for each model, “X” means the full continuity-diffusion equation is solved for the species, “F” means it is treated as being in photochemical equilibrium, “A” means it is an aerosol and falls out of the atmosphere, “C” means it is treated as chemically inert, and “–” means it is not included in that model. Note that boundary conditions like dry deposition velocity are not relevant for type F species, since transport is not included for such species. The exclusion of a species from a model does not necessarily mean that the model is incapable of simulating the species, just that it was not included in the atmospheric scenario selected here. For example, following Hu et al. (2012), the Hu model was deployed here without N species because the planet scenario selected here precludes reactive N, though it is capable of simulating nitrogenous chemistry. (2) For the bottom boundary condition, either a surface flux or a surface mixing ratio is specified. In the Kasting model and ATMOS,  $\text{N}_2$  is a special case; in these models,  $[\text{N}_2]$  is adjusted to set the total dry pressure of the atmosphere to be 1 bar (to account for outgassed species and photochemical intermediates). Consequently,  $p\text{N}_2 \lesssim 0.1$  bar in these models. (3) top-of-the-atmosphere (TOA) flux refers to the magnitude of outflow at the TOA; hence, a negative number would correspond to an inflow.

## Appendix C Detailed Model Intercomparison

In this appendix, we enumerate the model differences that drove the divergent predictions of  $r_{\text{CO}}$ . Some of these differences were errors; we discuss them below and summarize their correction in Table C1.

### C.1. $\text{CO}_2$ and $\text{H}_2\text{O}$ Cross Sections

Our model intercomparison reveals the single strongest control on  $r_{\text{CO}}$  to be treatment of the  $\text{H}_2\text{O}$  and  $\text{CO}_2$  cross sections. The abundance of CO in habitable planet atmospheres is photochemically controlled by a balance of  $\text{CO}_2$  photolysis, which generates CO, and  $\text{H}_2\text{O}$  photolysis, which is the ultimate source of the OH radicals that recombine CO and O to  $\text{CO}_2$  (see Section 2). The Hu model incorrectly implemented  $\text{CO}_2$  absorption. Specifically, Hu et al. (2012) approximated the absorption cross sections by the total extinction cross sections from Ityaksov et al. (2008). However, at wavelengths  $>201.58$  nm, the extinction cross section is dominated by scattering, and the absorption is  $\approx 0$ . Therefore, this error led to unphysical absorption from  $\text{CO}_2$  and suppression of the UV radiation field at  $\geq 202$  nm. This suppression was particularly acute because of the high scattering optical depth at  $\sim 200$  nm in the  $\text{CO}_2$ -dominated atmosphere, which amplified the unphysical absorption due to  $\text{CO}_2$  (Bohren 1987; Ranjan et al. 2017b). The  $\text{CO}_2$  absorption at  $\geq 204$  nm was not assumed to lead to photolysis, so  $\text{CO}_2$  photolysis itself was not overestimated due to this error.

Upon correction of the  $\text{CO}_2$  absorption cross sections, the atmosphere is largely transparent at wavelengths  $\geq 202$  nm, except for  $\text{H}_2\text{O}$ . Prior to this work, no experimentally measured or theoretically predicted absorption cross sections were available for  $\text{H}_2\text{O}(\text{g})$  at  $>198$  nm at conditions relevant to temperate rocky planets ( $T \sim 300$  K). The cross sections recommended by Burkholder et al. (2015), ultimately sourced from Parkinson et al. (2003), terminate at 198 nm due to lack of data. However, as originally pointed out by Kasting & Walker (1981), it is unphysical to assume that  $\text{H}_2\text{O}$  absorption should abruptly terminate at  $\sim 200$  nm. The dissociation energy of the

**Table C1**  
Required Corrections to the Models

Model	Correction
Hu	Removal of erroneous $>202$ nm $\text{CO}_2$ absorption (Appendix C.1)
ATMOS, Kasting	Correction of reaction network (Appendix C.2)
ATMOS	Use of self-consistent $T$ - $P$ - $\text{H}_2\text{O}$ Profile (Appendix C.3)

H–OH bond corresponds to photons of wavelength  $\sim 240$  nm, and photolysis should continue down to that wavelength, albeit at steadily lower cross sections. Consequently, models descended from Kasting & Walker (1981), in this study ATMOS and Kasting, extrapolate the  $\text{H}_2\text{O}$  cross sections from Thompson et al. (1963) out to longer wavelengths (Figure 2). This leads to  $\text{H}_2\text{O}$  photolysis and CO recombination at low altitudes (Harman et al. 2015). The Hu model originally used this extrapolation as well; however, due to the error in the  $\text{CO}_2$  cross sections,  $\text{H}_2\text{O}$  photolysis was suppressed at low altitudes, regardless of whether this extrapolation was included, and the Hu model eventually adopted the recommendation of Burkholder et al. (2015) for the  $\text{H}_2\text{O}$  cross sections.

If either the erroneous longwave  $\text{CO}_2$  absorption is present or the  $\text{H}_2\text{O}$  absorption extrapolation is neglected, then  $\text{H}_2\text{O}$  photolysis is suppressed and  $r_{\text{CO}}$  is high. The  $\text{CO}_2$  does not absorb  $>202$  nm, and in Section 3 we experimentally demonstrate that  $\text{H}_2\text{O}$  does indeed absorb at such wavelengths. Indeed, it absorbs larger cross sections than assumed by the ATMOS and Kasting models, meaning that  $\text{H}_2\text{O}$  photolysis, and hence CO recombination, is more intense than predicted by all three of the baseline models (Figure 2). Further, the latest data suggest that  $\text{CO}_2$  absorption terminates by 202 nm, shorter than all three of the models considered here, meaning that  $\text{CO}_2$  photolysis (and hence CO production) is lower than assumed by all three of the models (Figure C1). Therefore, CO should not only be lower than predicted by the baseline Hu model, it should be lower than predicted by all three of our models (Section 5).

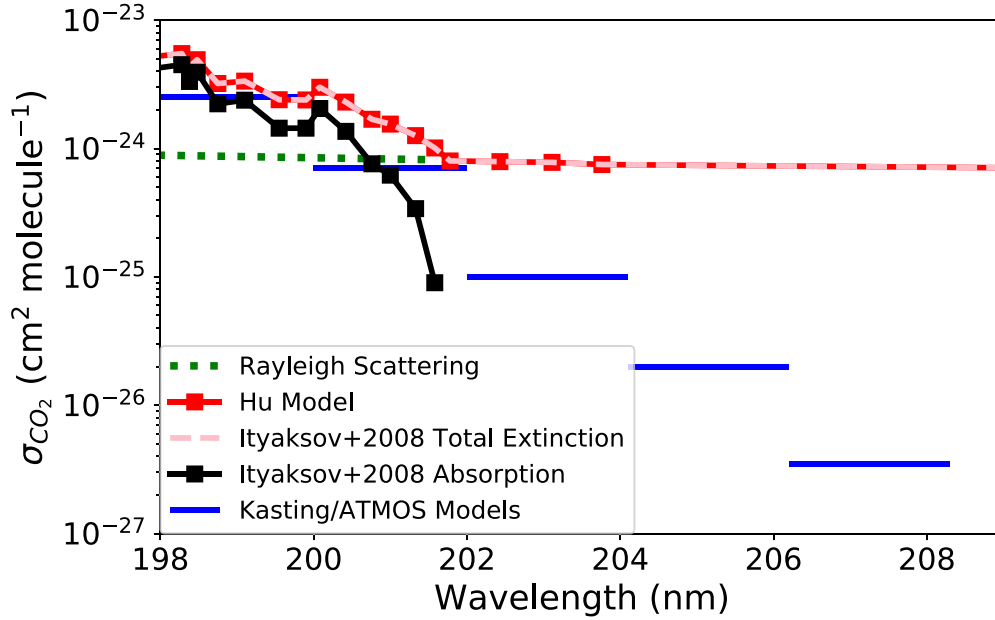


**Figure C1.** The  $\text{CO}_2$  absorption cross sections assumed by the Hu and ATMOS/Kasting models. The total extinction and absorption cross sections from Ityaksov et al. (2008) are also shown for reference, as is the  $\text{CO}_2$  Rayleigh scattering cross section calculated as in Ranjan & Sasselov (2017).

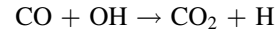
## C.2. Reaction Network

In our intercomparison, we found  $\text{SO}_2$  outgassing to suppress  $r_{\text{CO}}$  in ATMOS. The  $\text{SO}_2$  did not suppress  $r_{\text{CO}}$  in the Kasting model in the baseline scenario, but it did in the low-outgassing regime (zero  $\text{CH}_4$ ,  $\text{H}_2$  outgassing; Hu et al. 2012). We intercompared the Hu, Kasting, and ATMOS reaction networks, with particular emphasis on the sulfur chemistry. We identified a number of discrepancies in the Kasting and ATMOS models, summarized in Table C2. The discrepancies in the Kasting models were incorrect implementations of published reactions or rates. The discrepancies in ATMOS were the deactivation of known reactions; the rationale for these deactivations is not known. The primary effect of the correction of these discrepancies is to remove the effect whereby  $\text{SO}_2$  outgassing suppresses  $r_{\text{CO}}$  in all regimes evaluated in this study.

We note that differences persist between the reaction networks encoded in our models. Harman et al. (2015) encoded the reaction  $\text{HO}_2 + \text{SO}_2 \rightarrow \text{OH} + \text{SO}_3$ , following Graham et al. (1979). However, Graham et al. (1979) formally reported a nondetection of this reaction and an upper limit for the reaction rate. Hu et al. (2012) instead encoded the reaction  $\text{HO}_2 + \text{SO}_2 \rightarrow \text{O}_2 + \text{HSO}_2$  for the same reactants, following theoretical calculations by Wang & Hou (2005). Furthermore, Harman et al. (2015) included the reactions  $\text{SO} + \text{HO}_2 \rightarrow \text{SO}_2 + \text{OH}$  and  $\text{SO} + \text{HO}_2 \rightarrow \text{O}_2 + \text{HSO}$ , following DeMore et al. (1992). Yung & Demore (1982) proposed  $\text{SO} + \text{HO}_2 \rightarrow \text{SO}_2 + \text{OH}$  in analogy to  $\text{SO} + \text{ClO}$ . These reactions are not recommended in later versions of the JPL Evaluations (Sander et al. 2011); consequently, Hu et al. (2012) omitted them. Similarly, Harman et al. (2015) included the reaction  $\text{N} + \text{O}_3 \rightarrow \text{NO} + \text{O}_2$ , but ATMOS does not include this reaction, following the recommendation of Burkholder et al. (2015). These differences in reaction network did not affect the results in the scenarios studied in this paper but may be relevant to future work.

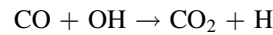
### C.2.1. CO + OH Rate Law

Hu, ATMOS, and Kasting encode different rate laws for the reaction of CO and OH. Hu encodes it as a two-body reaction, with rate law (Baulch et al. 1992 via NIST)



$$k = 5.4 \times 10^{-14} \left( \frac{T}{298 \text{ K}} \right)^{1.5} \exp \left( \frac{250.0 \text{ K}}{T} \right) \text{ cm}^3 \text{ s}^{-1}.$$

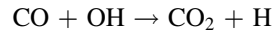
ATMOS also encodes it as a two-body reaction, with rate law (Sander et al. 2003)



$$k = 1.5 \times 10^{-13} \text{ cm}^3 \text{ s}^{-1} \times (1.0 + 0.6 \times P_{\text{atm}}),$$

where  $P_{\text{atm}}$  is the pressure in atmospheres.

Kasting encodes it following Sander et al. (2011). Note that the functional form linking  $k_{\text{inf}}$  and  $k_0$  to the rate constant  $k$  is different than the standard expression for three-body reaction rates:



$$k_0 = 1.5 \times 10^{-13} \text{ cm}^3 \text{ s}^{-1} \left( \frac{T}{300 \text{ K}} \right)^{0.6}$$

$$k_{\infty} = 2.1 \times 10^9 \text{ s}^{-1} \left( \frac{T}{300 \text{ K}} \right)^{6.1}$$

$$k = \left( \frac{k_0}{1 + \frac{k_0}{k_{\infty}/[M]}} \right) 0.6 \left[ 1 + \left( \log_{10} \left[ \frac{k_0}{k_{\infty}/[M]} \right] \right)^2 \right]^{-1}. \quad (\text{C1})$$

This differs slightly from the most recent JPL Chemical Kinetics Evaluation (Burkholder et al. 2015), where the exponent for the temperature dependence of  $k_0$  is zero rather than 0.6. For most terrestrial atmospheric applications, Burkholder et al. (2015) stated that this reaction rate can be approximated as bimolecular, with rate constant  $k \approx k_0 = 1.5 \times 10^{-13} \text{ cm}^3 \text{ s}^{-1}$ . This formalism falls intermediate to the ATMOS and Hu/Kasting formalisms, agreeing with ATMOS

**Table C2**  
Required Updates to Reaction Networks

Reaction	Old Parameter	Corrected Parameter	References
Kasting	...	...	...
$\text{SO}_2 + \text{O} + \text{M} \rightarrow \text{SO}_3 + \text{M}$	$k_0 = 1.8\text{E}-33(T/300 \text{ K})^{-2}; k_\infty = 4.2\text{E}-14(T/300 \text{ K})^{-1.8}$	$k_0 = 1.8\text{E}-33(T/300 \text{ K})^2; k_\infty = 4.2\text{E}-14(T/300 \text{ K})^{1.8}$	Sander et al. (2011)
$\text{SO} + \text{O}_3 \rightarrow \text{SO}_2 + \text{O}_2$	$k = 3.6\text{E}-12 \exp(-1100/T)$	$k = 3.4\text{E}-12 \exp(-1100/T)$	Sander et al. (2011)
$\text{HS} + \text{HO}_2 \rightarrow \text{H}_2\text{S} + \text{O}_2$		$\rightarrow \text{HSO} + \text{OH}$	Stachnik & Molina (1987)
$\text{S} + \text{CO}_2 \rightarrow \text{SO} + \text{CO}$	$k = 1.2\text{E}-11$	$k = 1.0\text{E}-20$	Yung & Demore (1982)
ATMOS	...	...	...
$^3\text{CH}_2 + \text{H}_2 \rightarrow \text{CH}_3 + \text{H}$	$k = 0$	$k = 5.0\text{E}-14$	Harman et al. (2015)
$^3\text{CH}_2 + \text{CH}_4 \rightarrow \text{CH}_3 + \text{CH}_3$	$k = 0$	$k = 7.1\text{E}-12 \exp(-5051/T)$	Harman et al. (2015)
$\text{SO} + \text{HO}_2 \rightarrow \text{SO}_2 + \text{OH}$	$k = 0$	$k = 2.8\text{E}-11$	Harman et al. (2015)
$\text{HSO}_3 + \text{OH} \rightarrow \text{H}_2\text{O} + \text{SO}_3$	$k = 0$	$k = 1.0\text{E}-11$	Harman et al. (2015)
$\text{HSO}_3 + \text{H} \rightarrow \text{H}_2 + \text{SO}_3$	$k = 0$	$k = 1.0\text{E}-11$	Harman et al. (2015)
$\text{HSO}_3 + \text{O} \rightarrow \text{OH} + \text{SO}_3$	$k = 0$	$k = 1.0\text{E}-11$	Harman et al. (2015)
$\text{HS} + \text{O}_2 \rightarrow \text{OH} + \text{SO}$	$k = 0$	$k = 4.0\text{E}-19$	Harman et al. (2015)
$\text{HS} + \text{H}_2\text{CO} \rightarrow \text{H}_2\text{S} + \text{HCO}$	$k = 0$	$k = 1.7\text{E}-11 \exp(-800/T)$	Harman et al. (2015)
$\text{SO}_2 + \text{HO}_2 \rightarrow \text{SO}_3\text{S} + \text{OH}$	$k = 0$	$k = 1.0\text{E}-18$	Harman et al. (2015)
$\text{S} + \text{CO}_2 \rightarrow \text{SO} + \text{CO}$	$k = 0$	$k = 1.0\text{E}-20$	Yung & Demore (1982)
$\text{SO} + \text{HO}_2 \rightarrow \text{HSO} + \text{O}_2$	$k = 0$	$k = 2.8\text{E}-11$	Harman et al. (2015)
$\text{HSO} + \text{NO}_2 \rightarrow \text{HNO} + \text{SO}$	$k = 0$	$k = 1.0\text{E}-15$	Harman et al. (2015)



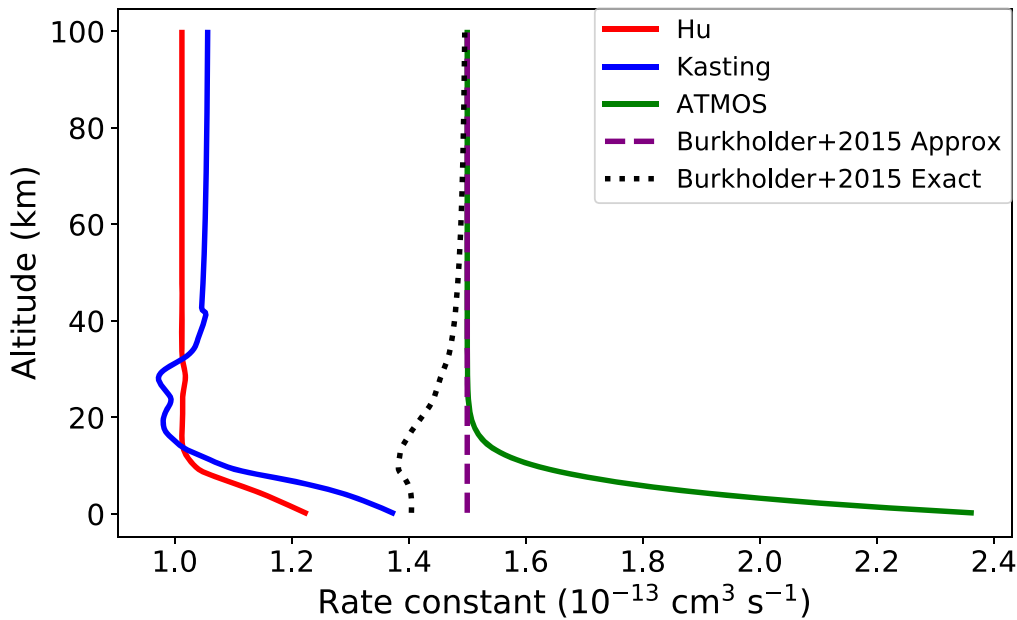


**Figure C2.** Different effective bimolecular rate laws for  $\text{CO} + \text{OH} \rightarrow \text{CO}_2 + \text{H}$  as a function of altitude in the  $T$ - $P$  profile corresponding to this planetary scenario, calculated by ATMOS (see Figure C3). The lower atmosphere, where the  $\text{H}_2\text{O}$  photolysis rate is high and this reaction most important, is also where these rate laws most strongly disagree.

in the upper atmosphere and Hu/Kasting in the lower atmosphere. Note that since most  $\text{H}_2\text{O}$  and hence OH production is in the lower atmosphere, the lower atmosphere is photochemically overweighted. Figure C2 presents the differing  $\text{CO} + \text{OH}$  rate laws used in our models as a function of altitude for the temperature–pressure profile considered in this study. In sum, variation in the  $\text{CO} + \text{OH}$  rate law can affect  $r_{\text{CO}}$  by 1.5–2 $\times$ , and the most recently proposed rate law (from Burkholder et al. 2015) is intermediate to the rate laws used to date.

### C.2.2. $\text{S} + \text{CO}$ Rate Law

ATMOS includes the reaction  $\text{S} + \text{CO} + \text{M} \rightarrow \text{OCS} + \text{M}$ , with a rate law equal to that of  $\text{O} + \text{CO} + \text{M} \rightarrow \text{CO}_2 + \text{M}$ , following Mills (1998). This reaction has not been observed in the laboratory but has been included because it is inferred from the atmospheric photochemistry of Venus, particularly the presence of OCS in its lower atmosphere (Krasnopolsky 2007; Yung et al. 2009). Inclusion of this reaction decreases  $r_{\text{CO}}$  by 20% and supports  $\sim$ ppb levels of OCS. When this reaction is excluded, OCS essentially does not exist in the atmospheric scenarios we consider here. We identify this reaction as a key target for experimental characterization.

### C.3. Atmospheric Profile

In anoxic, abiotic  $\text{CO}_2$ -rich atmospheres, the stratosphere is cold due to efficient line cooling by  $\text{CO}_2$  and the absence of shortwave-absorbing stratospheric  $\text{O}_3$  (from biogenic  $\text{O}_2$ ) or haze (from biogenic  $\text{CH}_4$ ; Kasting et al. 1984; Roble 1995; Wordsworth & Pierrehumbert 2013; Rugheimer & Kaltenegger 2018). Cold stratospheres are dry, due to the low saturation pressure of  $\text{H}_2\text{O}$  at low temperatures (Wordsworth & Pierrehumbert 2013). If this fact is neglected (i.e., if the stratosphere is allowed to be relatively warm and moist), then vigorous  $\text{H}_2\text{O}$  photolysis in the wet upper atmosphere generates abundant OH, which

suppresses  $r_{\text{CO}}$  regardless of assumptions on  $\text{H}_2\text{O}$  and  $\text{CO}_2$  cross sections. The baseline  $T$ - $P$  profile in the ATMOS Archaean+haze template is warm ( $\sim$ 230 K) because it was calculated for conditions in which shortwave absorption due to haze heats the stratosphere. By contrast, at the low  $\text{CH}_4/\text{CO}_2$  ratios expected for  $\text{CO}_2$ -dominated abiotic exoplanets, haze formation is not expected, and the stratosphere should be cold ( $\sim$ 150–170 K) and dry (DeWitt et al. 2009; Guzmán-Marmolejo et al. 2013; Arney et al. 2016). This means that when applying the Archaean+haze template from ATMOS to this planetary scenario, it is important to first recalculate temperature–pressure profiles that are consistent with this scenario, e.g., by using the CLIMA module of ATMOS (Figure C3). Neglect of self-consistent climate can lead to overestimating upper-atmospheric  $[\text{H}_2\text{O}]$  (and hence  $\text{H}_2\text{O}$  photolysis rates) by 2–4 orders of magnitude.

### C.4. $\text{H}$ and $\text{H}_2$ Escape Rates

Atmospheric  $\text{H}_2$  stabilizes CO by suppressing OH and O (Kasting et al. 1983; Kharecha et al. 2005). In abiotic, anoxic atmospheres,  $p_{\text{H}_2}$  is generally set by a balance between  $\text{H}_2$  outgassing and H and  $\text{H}_2$  escape from the atmosphere, with the escape velocities calculated by

$$v_{\text{diff}} = D \left( \frac{1}{H_0} - \frac{1}{H} \right), \quad (\text{C2})$$

where  $D(X, Y)$  is the molecular diffusion coefficient of  $X$  through  $Y$  in  $\text{cm}^2 \text{s}^{-1}$ ,  $H_0$  is the scale height for the bulk atmosphere at the escape altitude,  $H$  is the scale height for the escaping component at the escape altitude, and  $v_{\text{diff}}$  is the diffusion-limited escape velocity.

The calculations of  $D(X, Y)$  for H and  $\text{H}_2$  through  $\text{CO}_2$  and  $\text{N}_2$  are different between the Hu, Kasting, and ATMOS models (Figure C4). Specifically, the Kasting model uses a generalized

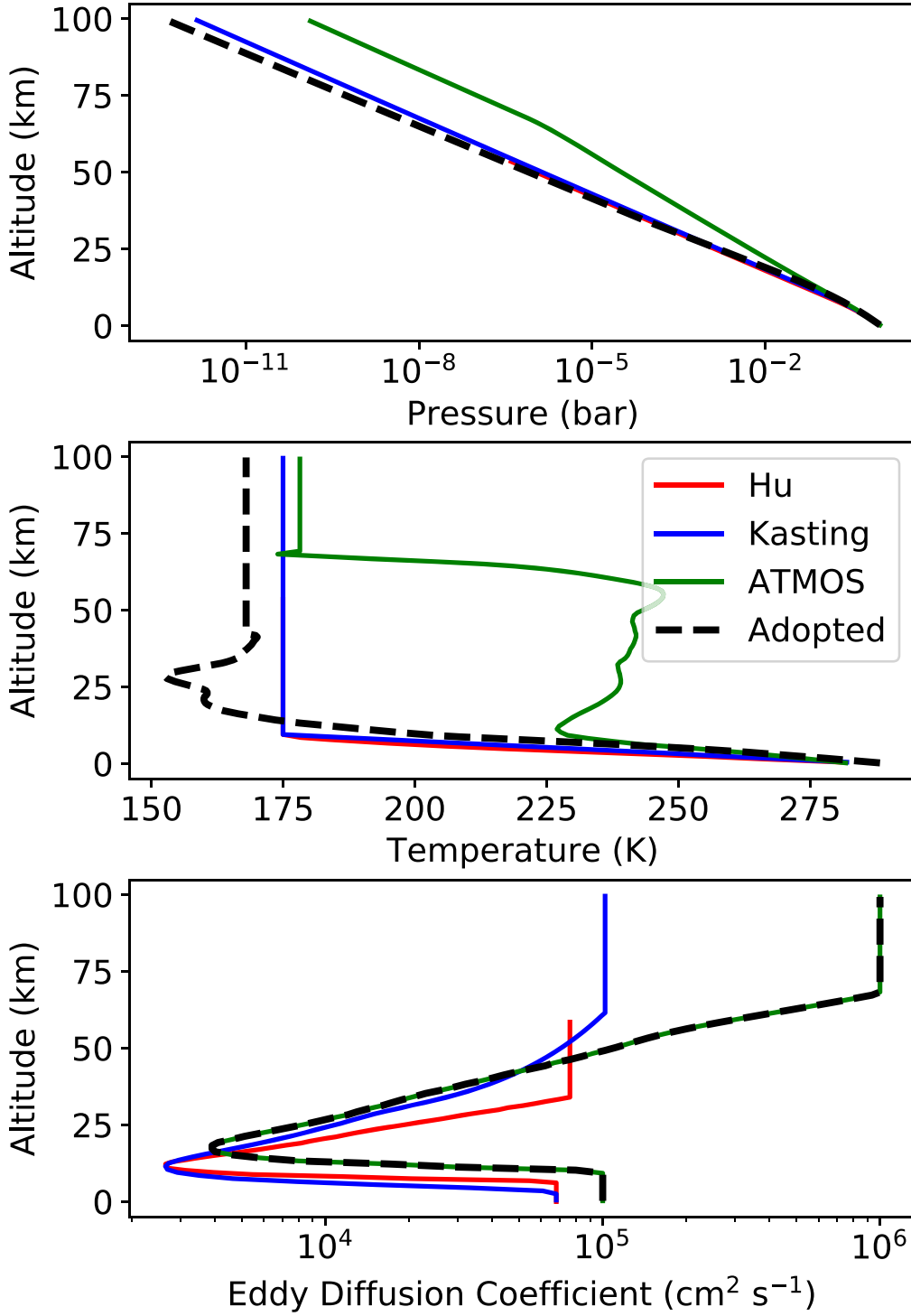


**Figure C3.** Pressure, temperature, and eddy diffusion coefficients as a function of altitude in the baseline models at project outset (solid colored lines; Hu et al. 2012; Harman et al. 2015; Arney et al. 2016). The original ATMOS  $T$ - $P$  profile was derived from an unconverged haze run. Dashed black lines give these profiles as self-consistently calculated by ATMOS for the particular planetary scenario we consider here; these are the profiles adopted for purposes of intercomparison (see Appendix C.5). It is crucial to include the cold stratosphere that results from the presence of  $\text{CO}_2$  and the lack of shortwave absorbers; otherwise, the upper atmosphere is moistened and the  $\text{H}_2\text{O}$  photolysis rate is unphysically enhanced.

diffusion coefficient formulation, valid for an interaction radius of  $3 \times 10^{-8}$  cm (Banks & Kockart 1973),

$$D_i = \frac{1.52 \times 10^{18} \times \left(\frac{1}{\mu} + \frac{1}{\bar{\mu}}\right)^{0.5} \times T^{0.5} \text{ cm}^{-1} \text{ s}^{-1}}{n}, \quad (\text{C3})$$

where  $\mu$  is the molecular weight of the individual species,  $\bar{\mu}$  is the mean molecular weight of the atmosphere,  $n$  is the number density in  $\text{cm}^{-3}$ , and  $T$  is the temperature in K.

The Hu model uses individualized expressions for  $D(X, Y)$ . The  $D(\text{H}, \text{N}_2)$  and  $D(\text{H}_2, \text{N}_2)$  are taken from Banks & Kockart (1973). The  $D(\text{H}_2, \text{CO}_2)$  is taken from Marrero & Mason (1972), with the caveat that the exponential correction factor

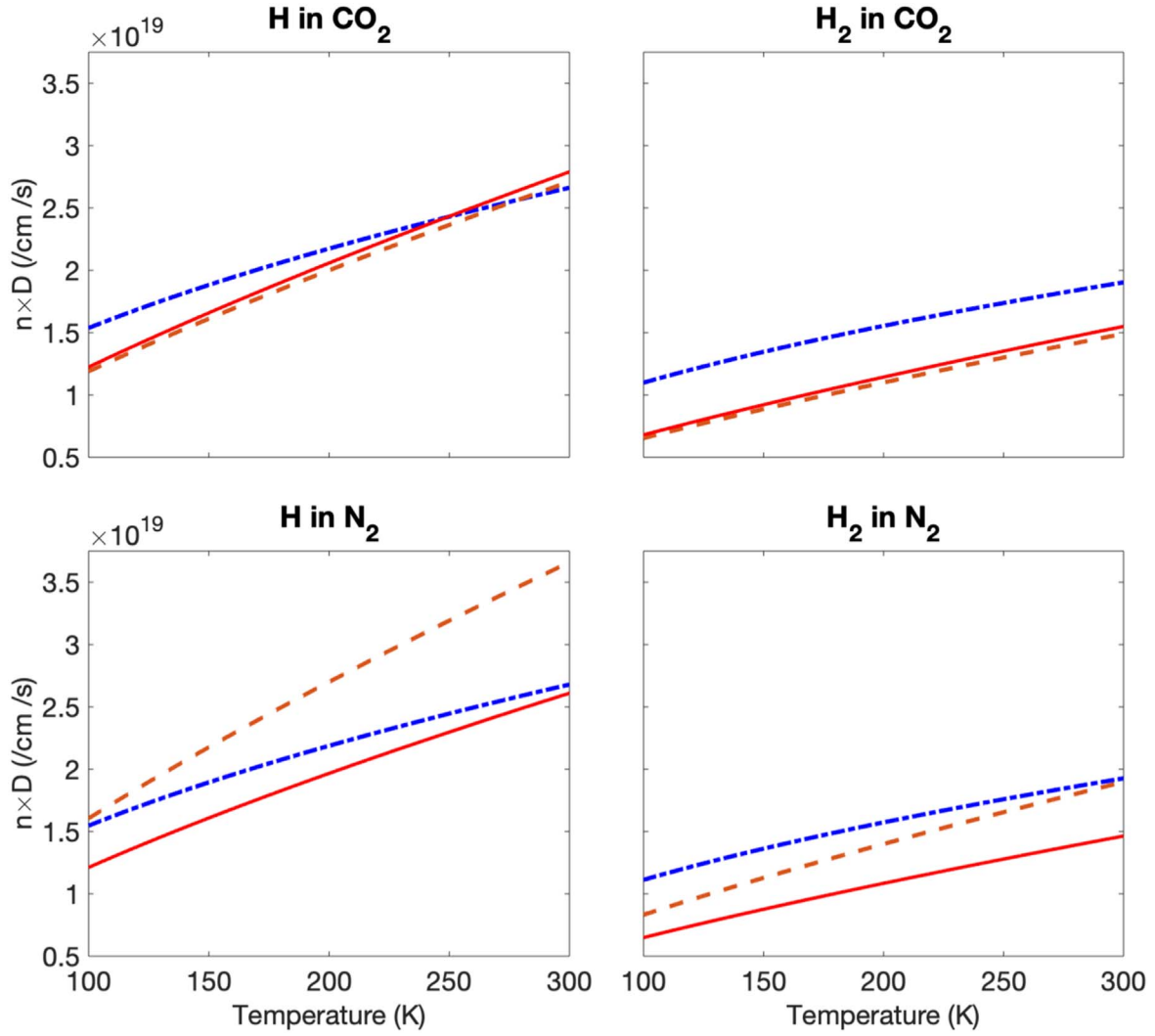


**Figure C4.** The  $nD(X, Y)$  from different models. Red curves correspond to the Hu model, blue to the Kasting model, and orange to ATMOS.

$\exp\left(\frac{-11.7\text{K}}{T}\right)$  is evaluated at 175 K, corresponding to the assumed stratospheric temperature in the  $\text{CO}_2$ -dominated case from Hu et al. (2012); this simplification leads to a  $<4\%$  deviation from 150 to 300 K. The  $D(\text{H}, \text{CO}_2)$  is taken as  $1.8 \times D(\text{H}_2, \text{CO}_2)$  following the observation of Zahnle et al. (2008) that  $D(\text{H}, \text{He}) = 1.8 \times D(\text{H}_2, \text{He})$ :

$$D(\text{H}, \text{CO}_2) = \frac{3.87 \times 10^{17} T^{0.75} \text{ cm}^{-1} \text{ s}^{-1}}{n}$$

$$D(\text{H}_2, \text{CO}_2) = \frac{2.15 \times 10^{17} T^{0.75} \text{ cm}^{-1} \text{ s}^{-1}}{n}$$

$$D(\text{H}, \text{N}_2) = \frac{4.87 \times 10^{17} T^{0.698} \text{ cm}^{-1} \text{ s}^{-1}}{n}$$

$$D(\text{H}_2, \text{N}_2) = \frac{2.15 \times 10^{17} T^{0.740} \text{ cm}^{-1} \text{ s}^{-1}}{n}.$$

The ATMOS model uses

$$D(\text{H}, \text{CO}_2) = \frac{2.0 \times 10^{19} (T/200 \text{ K})^{0.75}}{n}, \quad (\text{C4})$$

$$D(\text{H}_2, \text{CO}_2) = \frac{1.1 \times 10^{19} (T/200 \text{ K})^{0.75}}{n}, \quad (\text{C5})$$

$$D(\text{H}, \text{N}_2) = \frac{2.7 \times 10^{19} (T/200 \text{ K})^{0.75}}{n}, \quad (\text{C6})$$

$$D(\text{H}_2, \text{N}_2) = \frac{1.4 \times 10^{19} (T/200 \text{ K})^{0.75}}{n}. \quad (\text{C7})$$

Figure C4 shows the variation in diffusion coefficient as a function of temperature for the formalisms selected by the different models. Here  $nD$  does not vary significantly as a function of background gas for the Hu and Kasting models; however,  $nD$  varies significantly as a function of background gas in ATMOS. By default, ATMOS uses coefficients for diffusion through  $\text{N}_2$ . Correcting these to the coefficients for diffusion through  $\text{CO}_2$  (e.g., ATMOS “Mars” setting) results in a  $1.5\times$  increase in  $p\text{H}_2$  and a  $2\times$  increase for  $r_{\text{CO}}$ . For diffusion through  $\text{CO}_2$ , the Kasting formalism leads to higher escape of  $\text{H}_2$  (and hence lower  $p\text{H}_2$  and  $r_{\text{CO}}$ ) compared to the Hu and ATMOS models.

### C.5. Demonstrating Model Agreement

To demonstrate that we have identified the key parameters driving the published variation in  $r_{\text{CO}}$  between models, we run all three models under identical assumptions and show that our models agree and that we can reproduce both the high and low

**Table C3**Parameters Defining High- and Low-CO Cases (Hu et al. 2012 CO<sub>2</sub>-dominated Scenario) File

Scenario Parameter	High CO	Low CO
H <sub>2</sub> O cross sections (ATMOS/Kasting)	Terminated at 198 nm	Extrapolated to 208.3 nm
H and H <sub>2</sub> diffusion coefficient	Hu/ATMOS (CO <sub>2</sub> -dominated)	Kasting
CO + OH rate law	Hu/Kasting	ATMOS
S + CO	No	Yes <sup>a</sup>

**Note.**

<sup>a</sup> The Kasting model (Harman et al. 2015) does not include OCS and hence does not include this reaction.

**Table C4**

Parameters Held Constant between High- and Low-CO Cases

Scenario Parameter	Hu	ATMOS	Kasting
Semimajor axis		1.21 au	
<i>T</i> – <i>P</i> profile		Calculated from ATMOS (Figure C3)	
Eddy diffusion		ATMOS (Figure C3)	
Surface albedo		0.25	
CO <sub>2</sub> cross sections		As in Kasting/ATMOS (Kasting & Walker 1981)	
Vertical resolution		0–100 km, 1 km resolution	
Lightning		Off	
Rainout		10 <sup>−9</sup> × Earth-like	
Global redox balance enforced	No	No	No/Yes

$r_{\text{CO}}$  published in the literature. Table C3 enumerates the conditions required to achieve high and low CO in our models. Table C4 lists the other parameters that must be aligned between the models. We note that the choices of the constant parameters (Table C4) are chosen primarily to facilitate the numerical experiment of the intercomparison, not for physical realism. For example, we essentially neglect rainout for purposes of this intercomparison; we do this not because CO<sub>2</sub>-dominated rocky planets should lack rain, but because this is the most tractable rainout regime we can force all three of our models into and the results are not sensitive to this assumption. Similarly, when considering CO<sub>2</sub> absorption, we use cross sections from the Kasting/ATMOS models, not because they are the most current estimates of CO<sub>2</sub> absorption, but because it is easier to incorporate these cross sections into the Hu model than vice versa. Finally, we note that while mixing-length theory suggests that the CO<sub>2</sub>-dominated atmospheres should be more turbid than N<sub>2</sub>-dominated atmospheres (Hu et al. 2012; Harman et al. 2015), using the Hu et al. (2012) eddy diffusion profile for CO<sub>2</sub>-dominated atmospheres leads to numerical instabilities in the ATMOS and Kasting models. We consequently elect to use the ATMOS eddy diffusion profile, calibrated for N<sub>2</sub>-dominated atmospheres, in this numerical experiment. It is unclear why reduced eddy diffusion should lead to such instabilities; we intend further studies to answer this question. Overall, we therefore emphasize that the use of these parameters should not necessarily constitute an endorsement, as they were primarily chosen to facilitate model intercomparison. The models were corrected for the errors

**Table C5**CO Surface Mixing Ratios for the Three Models, Applied to Our Abiotic CO<sub>2</sub>–N<sub>2</sub> Atmospheric Scenario

Scenario Parameter	$r_{\text{CO}}$ (Hu)	$r_{\text{CO}}$ (ATMOS)	$r_{\text{CO}}$ (Kasting)
Initially	8.2E−3	1.72E−4	2.1E−4
Low-CO assumptions	2.7E−4	2.6E−4	1.3E−4/1.5E−4 <sup>a</sup>
High-CO assumptions	5.9E−3	5.4E−3	8.1E−3/8.2E−3 <sup>a</sup>


**Notes.** The first line presents the mixing ratios from the models at the outset of the project, i.e., prior to fixing the errors in Table C1. The  $r_{\text{CO}}$  disagreed by 50×. The second and third lines present the mixing ratios calculated from the models after fixing the errors, with uniform simulation parameters, under assumptions corresponding to both high and low CO (Tables C3 and C4). The calculated  $r_{\text{CO}}$  agreed within a factor of 2× between models, demonstrating that we had successfully identified and accounted for the factors driving divergent  $r_{\text{CO}}$  between models.

<sup>a</sup> Global redox balance enforced as per Harman et al. (2015).

summarized in Table C1, and the simulation parameters were otherwise as given in Tables A1 and B1.

The results of this numerical experiment are given in Table C5. Our models (1) agree with each other to within a factor of 2 and (2) can reproduce both the low (~200 ppm) and high (~8200 ppm) CO surface mixing ratios published in the literature (e.g., Hu et al. 2012; Harman et al. 2015). Agreement between ATMOS and Hu is within 10%, reflecting particularly intensive intercomparison. We conclude that we have successfully identified the parameters driving divergent predictions of  $r_{\text{CO}}$  in this planetary scenario.

**ORCID iDs**

Sukrit Ranjan  <https://orcid.org/0000-0002-5147-9053>  
Edward W. Schwieterman  <https://orcid.org/0000-0002-2949-2163>  
Chester Harman  <https://orcid.org/0000-0003-2281-1990>  
Alexander Fateev  <https://orcid.org/0000-0003-2863-2707>  
Clara Sousa-Silva  <https://orcid.org/0000-0002-7853-6871>  
Renyu Hu  <https://orcid.org/0000-0003-2215-8485>

**References**

- Ardaseva, A., Rimmer, P. B., Waldmann, I., et al. 2017, *MNRAS*, **470**, 187  
Arney, G., Domagal-Goldman, S. D., Meadows, V. S., et al. 2016, *AsBio*, **16**, 873  
Badr, O., & Probert, S. 1995, *ApEn*, **50**, 339  
Banks, P. M., & Kockart, G. 1973, *Aeronomy (Part B)* (New York: Academic)  
Batalha, N., Domagal-Goldman, S. D., Ramirez, R., & Kasting, J. F. 2015, *Icar*, **258**, 337  
Baulch, D., Cobos, C., Cox, R., et al. 1992, *JPCRD*, **21**, 411  
Benner, S. A., Kim, H.-J., & Biondi, E. 2019, *Life*, **9**, 84  
Bohren, C. F. 1987, *AmJPh*, **55**, 524  
Brogi, M., de Kok, R. J., Birkby, J. L., Schwarz, H., & Snellen, I. A. G. 2014, *A&A*, **565**, A124  
Burkholder, J., Abbatt, J., Huie, R., et al. 2015, *Chemical Kinetics and Photochemical Data for Use in Atmospheric Studies: Evaluation Number 18*, Tech. Rep., NASA Jet Propulsion Laboratory  
Cantrell, C. A., Zimmer, A., & Tyndall, G. S. 1997, *GeoRL*, **24**, 2195  
Catling, D. C., & Kasting, J. F. 2017, *Atmospheric Evolution on Inhabited and Lifeless Worlds* (Cambridge: Cambridge Univ. Press)  
Chan, W. F., Cooper, G., & Brion, C. E. 1993, *CP*, **178**, 387  
Chung, C.-Y., Chew, E. P., Cheng, B.-M., Bahou, M., & Lee, Y.-P. 2001, *NIMPA*, **467**, 1572  
Citron, R. L., Manga, M., & Hemingway, D. J. 2018, *Natur*, **555**, 643  
Cleaves, H. J. 2008, *PreR*, **164**, 111  
Darwent, B. d. B. 1970, *Bond Dissociation Energies in Simple Molecules*, Tech. Rep. 31, National Bureau of Standards (U.S.)



- DeMore, W., Sander, S., Golden, D., et al. 1992, JPL Publication 92-20, Tech. Rep. Evaluation 10
- DeWitt, H. L., Trainer, M. G., Pavlov, A. A., et al. 2009, *AsBio*, **9**, 447
- Dittmann, J. A., Irwin, J. M., Charbonneau, D., et al. 2017, *Natur*, **544**, 333
- Domagal-Goldman, S. D., Segura, A., Claire, M. W., Robinson, T. D., & Meadows, V. S. 2014, *ApJ*, **792**, 90
- Dressing, C. D., & Charbonneau, D. 2015, *ApJ*, **807**, 45
- France, K., Froning, C. S., Linsky, J. L., et al. 2013, *ApJ*, **763**, 149
- Fujii, Y., Angerhausen, D., Deitrick, R., et al. 2018, *AsBio*, **18**, 739
- Gaudi, B. S., Seager, S., Mennesson, B., et al. 2020, arXiv:2001.06683
- Gilbert, E. A., Barclay, T., Schlieder, J. E., et al. 2020, arXiv:2001.00952
- Gillon, M., Triaud, A. H. M. J., Demory, B.-O., et al. 2017, *Natur*, **542**, 456
- Graham, R. A., Winer, A. M., Atkinson, R., & Pitts, J. N. 1979, *JPhCh*, **83**, 1563
- Guzmán-Marmolejo, A., Segura, A., & Escobar-Briones, E. 2013, *AsBio*, **13**, 550
- Harman, C. E., Felton, R., Hu, R., et al. 2018, *ApJ*, **866**, 56
- Harman, C. E., Kasting, J. F., & Wolf, E. T. 2013, *OLEB*, **43**, 77
- Harman, C. E., Schwietzman, E. W., Schottelkotte, J. C., & Kasting, J. F. 2015, *ApJ*, **812**, 137
- Hu, R., & Diaz, H. D. 2019, *ApJ*, **886**, 126
- Hu, R., Peterson, L., & Wolf, E. T. 2020, *ApJ*, **888**, 122
- Hu, R., Seager, S., & Bains, W. 2012, *ApJ*, **761**, 166
- Ityaksov, D., Linnartz, H., & Ubachs, W. 2008, *CPL*, **462**, 31
- Jacob, D. J. 1999, Introduction to Atmospheric Chemistry (Princeton, NJ: Princeton Univ. Press)
- James, T., & Hu, R. 2018, *ApJ*, **867**, 17
- Kasting, J. F. 1990, *OLEB*, **20**, 199
- Kasting, J. F. 1993, *Sci*, **259**, 920
- Kasting, J. F. 2013, *ChGeo*, **362**, 13
- Kasting, J. F. 2014, *GSASP*, **504**, 19
- Kasting, J. F., Pollack, J. B., & Crisp, D. 1984, *JAiC*, **1**, 403
- Kasting, J. F., & Walker, J. C. 1981, *JGRC*, **86**, 1147
- Kasting, J. F., Zahnle, K. J., & Walker, J. C. G. 1983, *PreR*, **20**, 121
- Keller-Rudek, H., Moortgat, G. K., Sander, R., & Sørensen, R. 2013, *ESSD*, **5**, 365
- Kharecha, P., Kasting, J., & Siefert, J. 2005, *Geobiology*, **3**, 53
- Kopparapu, R. K., Ramirez, R., Kasting, J. F., et al. 2013, *ApJ*, **765**, 131
- Krasnopolsky, V. 2007, *Icar*, **191**, 25
- Krasnopolsky, V. A. 2011, *P&SS*, **59**, 952
- Krissansen-Totton, J., Olson, S., & Catling, D. C. 2018, *SciA*, **4**, ea05747
- Lightowers, P., & Cape, J. 1988, *AtmEn*, **22**, 7
- Lustig-Yaeger, J., Meadows, V. S., & Lincowski, A. P. 2019, *AJ*, **158**, 27
- LUVOIR Team 2019, arXiv:1912.06219
- Mancinelli, R. L., & McKay, C. P. 1988, *OrLi*, **18**, 311
- Marrero, T. R., & Mason, E. A. 1972, *JPCRD*, **1**, 3
- McElroy, M. B., & Donahue, T. M. 1972, *Sci*, **177**, 986
- Meadows, V. S., Reinhard, C. T., Arney, G. N., et al. 2018, *AsBio*, **18**, 630
- Meixner, M., Cooray, A., Leisawitz, D., et al. 2019, arXiv:1912.06213
- Mills, F. P. 1998, Dissertation (PhD), California Institute of Technology doi:10.7907/NWPG-E852
- Mills, F. P., & Allen, M. 2007, *P&SS*, **55**, 1729
- Mota, R., Parafita, R., Giuliani, A., et al. 2005, *CPL*, **416**, 152
- Parkinson, T. D., & Hunten, D. M. 1972, *JAiS*, **29**, 1380
- Parkinson, W., & Yoshino, K. 2003, *CP*, **294**, 31
- Parkinson, W. H., Rufus, J., & Yoshino, K. 2003, *CP*, **290**, 251
- Prinn, R. G. 1971, *JAiS*, **28**, 1058
- Prinn, R. G., & Fegley, B., Jr. 1987, *AREPS*, **15**, 171
- Quickenden, T., & Irvin, J. 1980, *JChPh*, **72**, 4416
- Ranjan, S., & Sasselov, D. D. 2017, *AsBio*, **17**, 169
- Ranjan, S., Todd, Z. R., Rimmer, P. B., Sasselov, D. D., & Babbin, A. R. 2019, *GGG*, **20**, 2021
- Ranjan, S., Wordsworth, R., & Sasselov, D. D. 2017a, *ApJ*, **843**, 110
- Ranjan, S., Wordsworth, R., & Sasselov, D. D. 2017b, *AsBio*, **17**, 687
- Reinhard, C. T., Olson, S. L., Schwietzman, E. W., & Lyons, T. W. 2017, *AsBio*, **17**, 287
- Ren, T., Modest, M. F., Fateev, A., & Clausen, S. 2015, *JQSRT*, **151**, 198
- Rimmer, P. B., & Helling, C. 2016, *ApJS*, **224**, 9
- Rimmer, P. B., & Rugheimer, S. 2019, *Icar*, **329**, 124
- Roble, R. 1995, *RvGeo*, **33**, 539
- Rodler, F., & López-Morales, M. 2014, *ApJ*, **781**, 54
- Rugheimer, S., & Kaltenecker, L. 2018, *ApJ*, **854**, 19
- Rugheimer, S., Kaltenecker, L., Segura, A., Linsky, J., & Mohanty, S. 2015a, *ApJ*, **809**, 57
- Rugheimer, S., Segura, A., Kaltenecker, L., & Sasselov, D. 2015b, *ApJ*, **806**, 137
- Sander, S. P., Friedl, R. R., Barker, J. R., et al. 2011, Chemical Kinetics and Photochemical Data for Use in Atmospheric Studies Evaluation Number 17, Tech. Rep. 17, NASA JPL, <http://jpldataeval.jpl.nasa.gov/>
- Sander, S. P., Friedl, R. R., Ravishankara, A. R., et al. 2003, Chemical Kinetics and Photochemical Data for Use in Atmospheric Studies Evaluation Number 14, Tech. Rep. 14, NASA JPL, <http://jpldataeval.jpl.nasa.gov/>
- Sandor, B. J., & Clancy, R. T. 2018, *Icar*, **313**, 15
- Sasselov, D. D., Grotzinger, J. P., & Sutherland, J. D. 2020, *SciA*, **6**, eaax3419
- Schaefer, L., & Fegley, B. J. 2011, *ApJ*, **729**, 6
- Schulz, C., Koch, J., Davidson, D., Jeffries, J., & Hanson, R. 2002, *CPL*, **355**, 82
- Schwietzman, E. W., Meadows, V. S., Domagal-Goldman, S. D., et al. 2016, *ApJL*, **819**, L13
- Schwietzman, E. W., Reinhard, C. T., Olson, S. L., et al. 2019, *ApJ*, **874**, 9
- Segura, A., Kasting, J. F., Meadows, V., et al. 2005, *AsBio*, **5**, 706
- Segura, A., Meadows, V. S., Kasting, J. F., Crisp, D., & Cohen, M. 2007, *A&A*, **472**, 665
- Shkolnik, E. L., & Barman, T. S. 2014, *AJ*, **148**, 64
- Snellen, I. A. G., de Kok, R. J., de Mooij, E. J. W., & Albrecht, S. 2010, *Natur*, **465**, 1049
- Stachnik, R., & Molina, M. 1987, *JPhCh*, **91**, 4603
- Tan, K. H., Brion, C. E., van der Leeuw, P. E., & van der Wiel, M. J. 1978, *CP*, **29**, 299
- Thompson, B., Harteck, P., & Reeves, R., Jr. 1963, *JGR*, **68**, 6431
- Tian, F., France, K., Linsky, J. L., Mauas, P. J. D., & Vieytes, M. C. 2014, *E&PSL*, **385**, 22
- Torres, G., Kipping, D. M., Fressin, F., et al. 2015, *ApJ*, **800**, 99
- Walker, J. C. 1974, *AmJS*, **274**, 193
- Wang, B., & Hou, H. 2005, *CPL*, **410**, 235
- Wang, Y., Tian, F., Li, T., & Hu, Y. 2016, *Icar*, **266**, 15
- Way, M. J., del Genio, A. D., Kiang, N. Y., et al. 2016, *GeoRL*, **43**, 8376
- Wogan, N. F., & Catling, D. C. 2020, *ApJ*, **892**, 127
- Wolf, E. T. 2017, *ApJL*, **839**, L1
- Wong, M. L., Charney, B. D., Gao, P., Yung, Y. L., & Russell, M. J. 2017, *AsBio*, **17**, 975
- Wordsworth, R., & Pierrehumbert, R. 2014, *ApJL*, **785**, L20
- Wordsworth, R. D. 2016, *AREPS*, **44**, 381
- Wordsworth, R. D., & Pierrehumbert, R. T. 2013, *ApJ*, **778**, 154
- Yung, Y. L., & Demore, W. B. 1982, *Icar*, **51**, 199
- Yung, Y. L., Liang, M. C., Jiang, X., et al. 2009, *JGR*, **114**, E00B34
- Zahnle, K., Haberle, R. M., Catling, D. C., & Kasting, J. F. 2008, *JGRE*, **113**, E11004